Design Synthesis of Nitrogen-Doped TiO_2@Carbon Nanosheets toward Selective Nitroaromatics Reduction under Mild Conditions

Xiaoyang Pan[1], Xiang Gao[2], Xuxing Chen[1], Ho Nyung Lee[2], Yun Liu[3], Ray L. Withers[3] and Zhiguo Yi[*1,4]*

[1]CAS Key Laboratory of Design and Assembly of Functional Nanostructures & Fujian Provincial Key Laboratory of Nanomaterials, Fujian Institute of Research on the Structure of Matter, Chinese Academy of Sciences, Fuzhou 350002, China.

[2]Materials Science and Technology Division, Oak Ridge National Laboratory, Oak Ridge, TN 37831, USA

[3]Research School of Chemistry, The Australian National University, ACT 2601, Australia

[4]University of Chinese Academy of Sciences, Beijing 100049, China

Abstract: The development of a facile and low-cost approach to the synthesis of aromatic amines remains a great scientific challenge. TiO_2, as a low-cost and earth abundant metal oxide, is usually not active for thermo-catalyzed nitro reduction. Herein, we report a composite nanosheet catalyst, composed of nitrogen-doped TiO_2

* Email: zhiguo@fjirsm.ac.cn

and carbon (N-TiO_2@C), which exhibits highly efficient, thermo-catalytic performance for selective nitroaromatic reduction at room temperature. The N-TiO_2@C nanosheet catalyst is synthesized via a facile approach where C_3N_4 nanosheets are utilized not only as a structure-directing agent to control the shape, size and crystal phase of TiO_2, but also as a source of nitrogen for doping into both TiO_2 and carbon nanosheets. Furthermore, the origin of the superior performance of the N-TiO_2@C nanosheet composite catalyst, along with a possible nitroaromatic reduction mechanism, has also been explored.

Keywords: Nitro reduction; noble metal free; TiO_2; nitrogen doping; nanosheets.

Introduction.

Aromatic amines, synthesized by selective reduction of nitroaromatics, are important intermediates for the manufacturing of various fine chemicals.[1-12] Traditionally, these compounds are produced by non-catalytic processes involving stoichiometric Fe or Zn reagents in the presence of various proton sources,[13-14] or by other catalytic protocols employing heterogeneous copper, nickel or platinum-group metals.[1-2, 4] These manufactures, however, are increasingly required to reduce the environmental impact of their processes and to increase their feedstock and energy efficiency.[2] To realize green and economical synthesis of aromatic amines, various attempts have been carried out to update the catalytic nitro reduction processes and catalysts.[5-9, 15-21] Among them, the hydrogenation reactions involving H_2 gas has potential to be applied in industry because of the economy hydrogen. However,

storage of hydrogen and highly pressurized conditions are disadvantages for this approach.[18] By contrast, the hydrogenation reactions involving $NaBH_4$ is less feasible for industrial application. However, this approach has the merit of mild reaction conditions[11, 22-23] and thus is suitable for small scale application in laboratory. Currently, the H_2 and $NaBH_4$ based catalytic reactions are both under intensive research,[5-9, 11, 17-18, 21-24] and most of the catalysts developed depend strongly on noble-metal catalysts, which suffer many critical problems including the prohibitive cost and scarcity of noble metals, agglomeration trends and low durability.[7, 17] It is therefore highly desirable to develop efficient, stable and cost-effective catalysts based on earth-abundant elements to catalyze the selective reduction of nitroaromatics.

Titanium dioxide, as an earth abundant, low cost and high stability semiconductor, has been widely used as a photocatalyst for a variety of applications.[25-26] Recently, it has been reported that TiO_2 nanomaterials can have excellent photoactivities and high selectivities under UV light irradiation for the selective reduction of a wide range of nitroaromatics.[10, 12, 15-16, 19, 27] The defect sites of the TiO_2 have been demonstrated to be the active sites for nitroaromatic adsorption and thus facilitate the subsequent reduction reactions.[19] Due to its unique properties for activating nitro groups, TiO_2 is also often used as the supporting substrate for noble metal nanoparticles and can thereby dramatically increase the chemoselectivity of noble metal catalysts for nitro reduction.[28-29] As a transition metal oxide, however,

without light irradiation or precious metal loading, TiO_2 is totally inactive for nitro reduction.

In view of the fact that heteroatoms doping can engineer the physicochemical properties of target materials[30-35] and two-dimensional nanostructures[36-38] with high specific surface areas and large fraction of uncoordinated surface atoms would be beneficial for catalytic reactions, we report herein the design synthesis of 2D TiO_2@carbon composite nanostructures with nitrogen doping (N-TiO_2@C) and their application as a catalyst for selective nitro reduction. It is found that the nitrogen doped, defective, composite nanosheets produced have unexpected superior activity, excellent stability as well as high selectivity for room temperature nitro reduction without the need for light illumination, resulting from its nitrogen doped, 2D architecture and defect-mediated nitro reduction mechanism.

Results and Discussion.

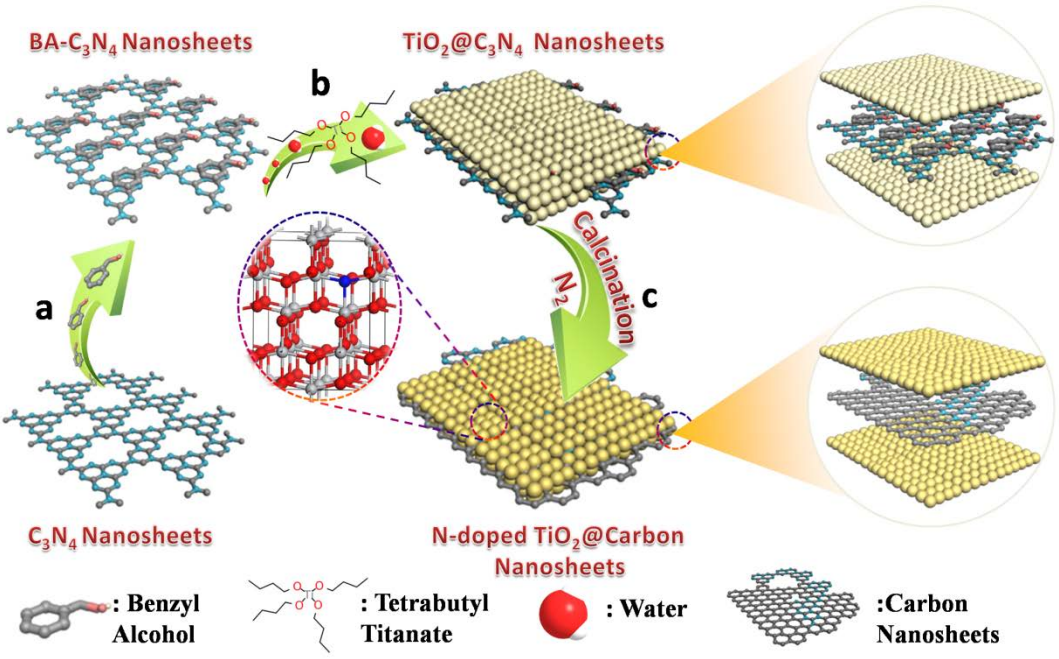

Figure 1. Schematic illustration for the synthesis of nitrogen-doped TiO_2–carbon (N-TiO_2@C) composite nanosheets. (**a**) Functionalizing C_3N_4 with benzyl alcohol (BA) via π-π interaction. (**b**) Reacting the BA functionalized C_3N_4 nanosheets with tetrabutyl titanate and water in ethanol solution to form amorphous titanium oxide sheets on the C_3N_4 template (TiO_2@C_3N_4). (**c**) Annealing the TiO_2@C_3N_4 sample at high temperature under a N_2 atmosphere.

Synthesis and characterization. The synthetic strategy for producing the N-TiO_2@C composite nanosheets is shown in Figure 1. First, C_3N_4[36, 39] nanosheets (Figure S1) were functionalized with benzyl alcohol (BA) via π-π interaction to facilitate the uniform coating of TiO_2. Then, the BA functionalized C_3N_4 nanosheets were reacted with tetrabutyl titanate and water in ethanol solution to form amorphous titanium oxide sheets on the C_3N_4 template (TiO_2@C_3N_4). After that, the as-obtained sample was subsequently heated up to 1073 K under a N_2 atmosphere for 4 hours. During this process, the thermal treatment induced crystallization of the amorphous titania nanosheets. Simultaneously, nitrogen (N) atoms decomposed from the C_3N_4 were doped into the lattice of TiO_2 and the BA functionalized C_3N_4 nanosheets were converted into N-doped carbon nanosheets. As a result, nitrogen-doped, TiO_2@carbon composite nanosheets (N-TiO_2@C) were obtained. For comparison purpose, TiO_2 nanosheets without carbon (TiO_2-NS) were also prepared by calcining the TiO_2@C_3N_4 under an O_2 atmosphere at 723K (Figure S2), and, blank TiO_2 (TiO_2-B) was synthesized using the same procedure as that of N-TiO_2@C but without adding the C_3N_4 template.

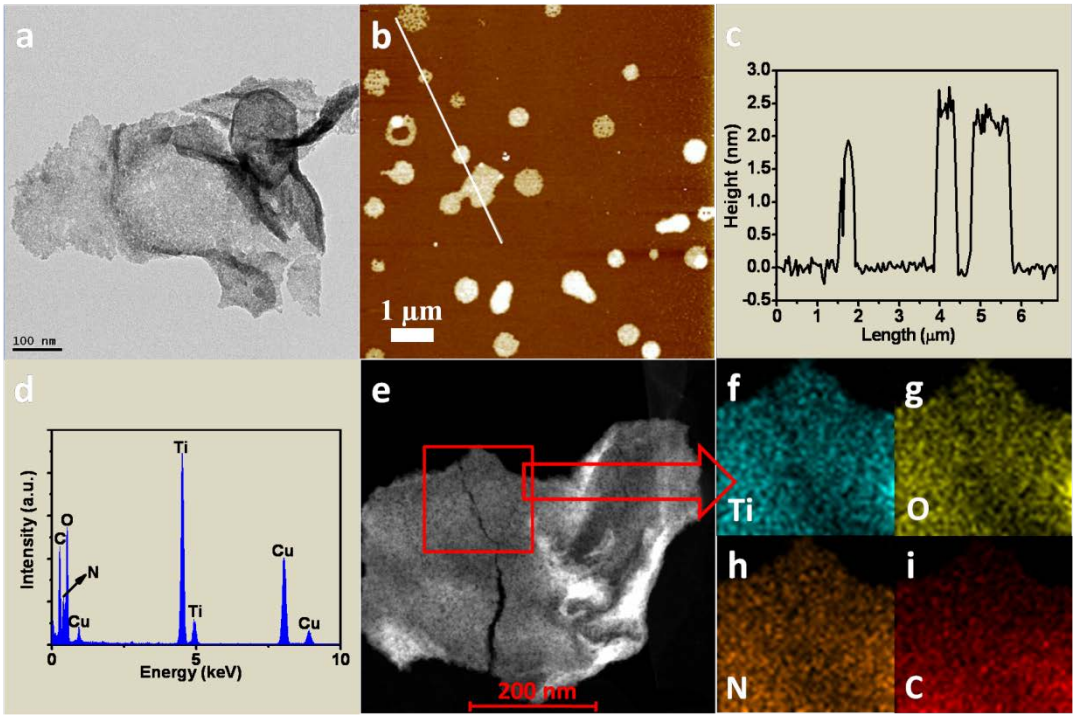

Figure 2. Physical Characterization of the N-TiO_2@C nanosheets. (**a**) TEM image. (**b**) AFM image. (**c**) Height profile along the line in (**b**). (**d**) EDX spectrum. (**e**) High angle annular dark field-scanning transmission electron microscopy (HAADF-STEM) image. (**f-i**) Elemental mapping patterns of Ti, O, N and C, respectively.

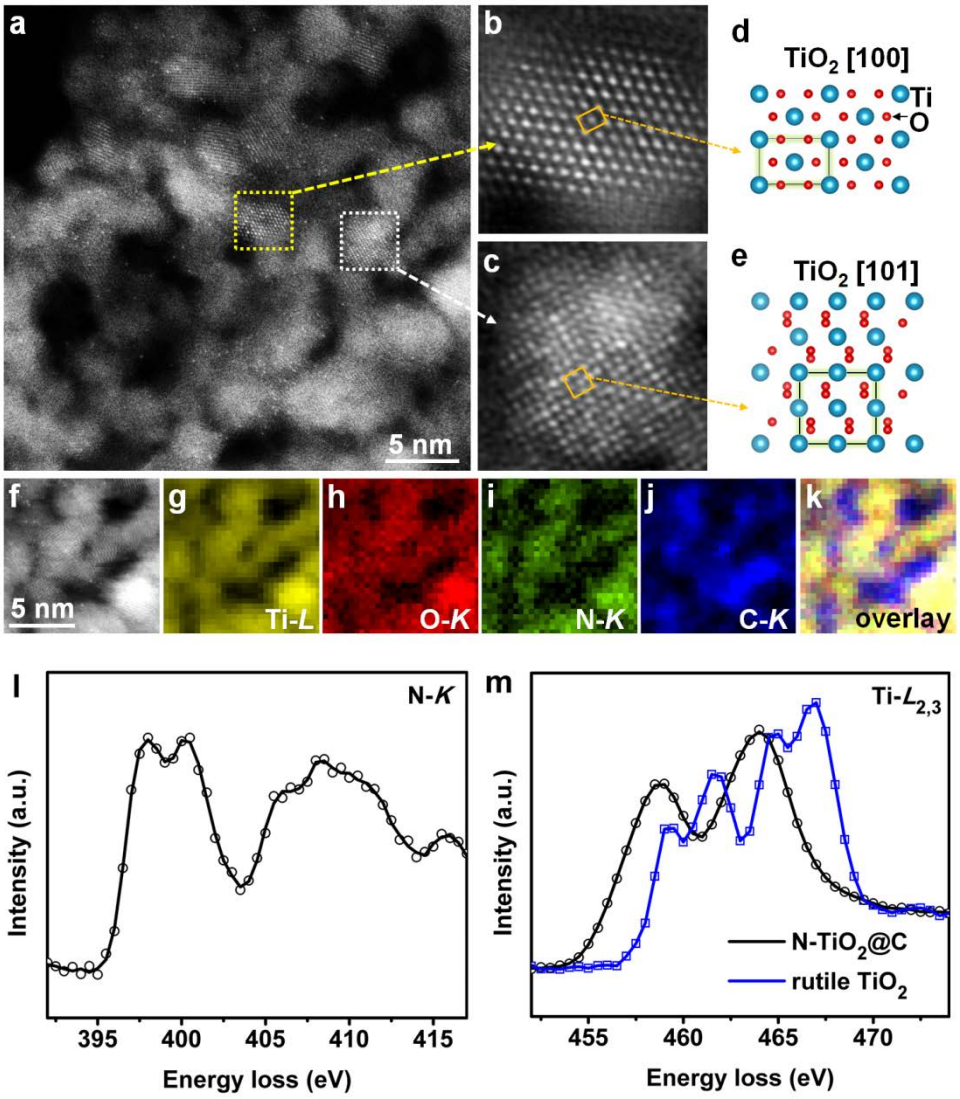

Figure 3. High resolution analysis of the N-TiO_2@C nanosheets. (**a**) HAADF-STEM image. (**b** and **c**) Magnified HAADF images obtained from two edge-on nanoparticles and (**d** and **e**) the corresponding atomic configurations. (**f**) HAADF-STEM image and (**g-k**) EELS elemental mapping patterns of Ti-*L*, O-*K*, N-*K*, C-*K* and their overlay. (**l** and **m**) EELS spectra of the N-*K* edge and Ti-*L* edge of N-TiO_2@C, respectively.

The morphology and microstructure of the N-TiO_2@C composite nanosheets were investigated by transmission electron microscopy (TEM) and atomic force

microscopy (AFM). As shown in Figure 2a, N-TiO_2@C possesses a wrinkled sheet morphology similar to that of the C_3N_4 template, in distinct contrast with the irregular TiO_2-B particles prepared without the C_3N_4 template (Figure S3). The carbon nanosheets can be clearly idendified at the edge of TiO_2 nanosheets, as shown in Figure S4a-d. AFM analyses indicate that the N-TiO_2@C composite nanosheets have a thickness varying from 2.0 to 2.5 nm (Figure 2 b and c). Energy-dispersive X-ray (EDX) analysis (Figure 2d) shows that the N-TiO_2@C composite contains the elements Ti, O, N and C with atomic ratios of 1.0 : 1.6 : 0.19 : 2.09 (Table S1). The elemental mapping analysis (Figure 2 e-i) suggests that the elements of Ti, O, N and C are homogeneously distributed in the N-TiO_2@C nanosheets.

To further understand the structure of N-TiO_2@C, analyses of high-resolution STEM imaging and EELS elemental mapping were performed. The Z-contrast (where Z refers to atomic number) HAADF image shown in Figure 3a indicates that the N-TiO_2@C nanosheets contain a high concentration of small nanoparticles that are uniformly 3-5 nm in size. Figure 3 b and c exhibit magnified high-angle annular dark-field (HAADF) images obtained from two edge-on nanoparticles, which match well with the projection of the rutile TiO_2 structure along its [100] and [101] zone axis directions (Figure 3 d and e). Note that the light O (Z = 8) and N (Z = 7) atoms have a weak ability to scatter electrons to high angles and hence are barely visible in the HAADF image. EELS mapping further reveals that the nanoparticles are composed of uniformly distributed, Ti, O and N elements (Figure 3 f-i). These results confirm that the nanosheets are composed of nitrogen-doped TiO_2 nanoparticles interconnected to

form an overall porous structure. The EELS elemental mapping analysis shows also that the element carbon is concentrated in the interspace regions of the nitrogen-doped TiO_2 nanoparticles (Figure 3 i-k), where the N signal is rather weak, indicating that most of the N are doped into the TiO_2 structure.

Figure 3 l and m show the fine structures of the background subtracted, N-*K* edge and Ti-$L_{2,3}$ edge EELS profiles obtained from the N-doped nanoparticles. The N-*K* edge exhibits a double-peak structure between ~395 and ~403 eV (Figure 3l), characteristic of N doped TiO_2 and can be ascribed to N replacing O in the TiO_2 structure.[30] This substitution explains why the TiO_2 containing a high concentration of N dopants (roughly ~9 at % according to the EDX quantification analysis) can retain its parent rutile structure (Figure S4d). However, due to the additional negative charge caused by the N^{3-}/O^{2-} replacements, compensating vacancies on the O^{2-} sites also need to form. As a result, a decrease in the average valence state of Ti in the doped nanoparticles is expected. This is exactly what was observed: the N doped nanoparticles display an obvious chemical shift in the Ti-$L_{2,3}$ edge as compared to that obtained from single crystalline rutile TiO_2 (Figure 3m), indicating the presence of considerable Ti^{3+} as well as oxygen vacancies in the N doped TiO_2 nanoparticles.[40]

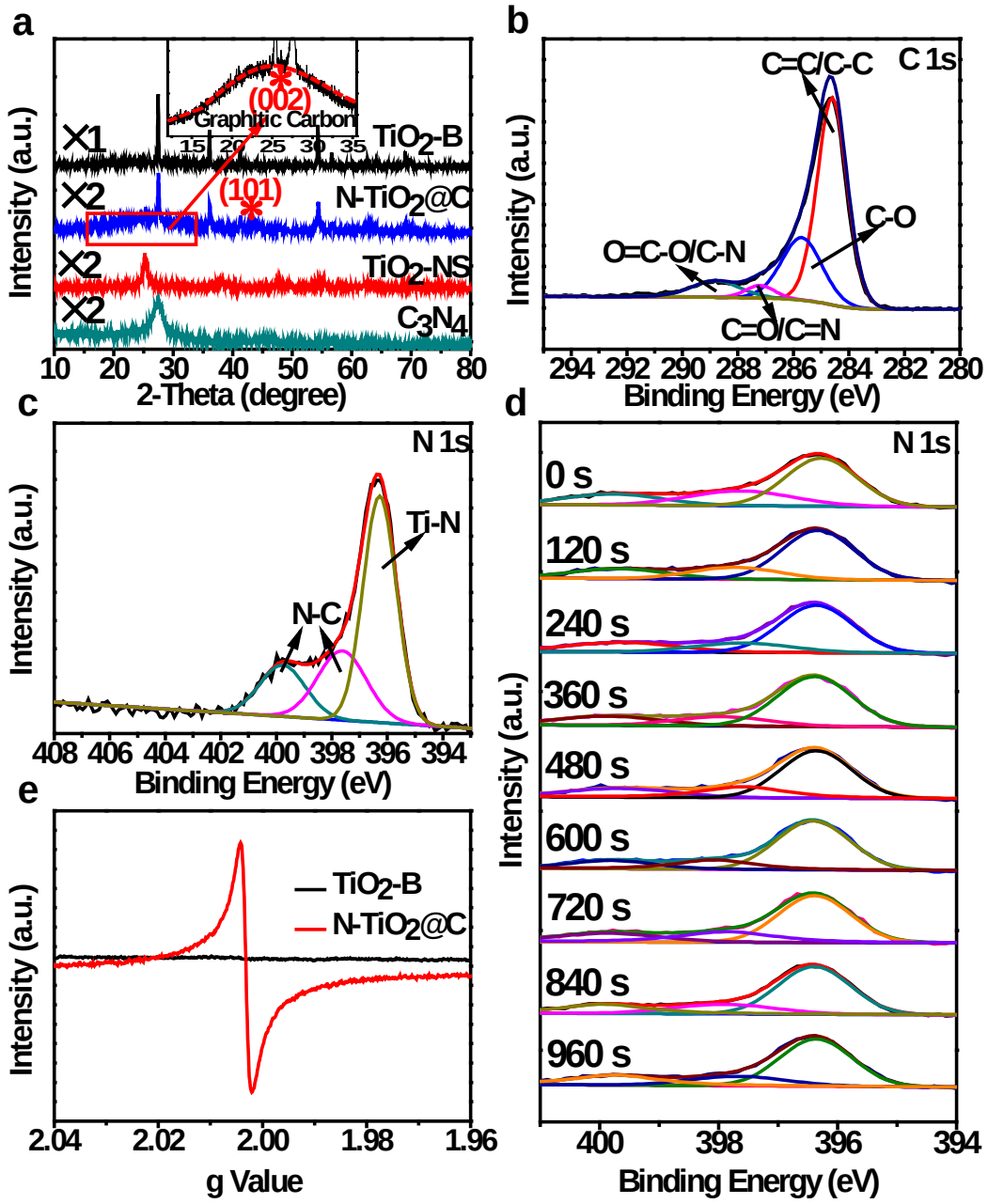

Figure 4. Structure and composition analysis of the as-prepared samples. (**a**) The XRD patterns of the C_3N_4, blank TiO_2 (TiO_2-B), TiO_2 nanosheets (TiO_2-NS) and N-TiO_2@C nanosheets. (**b** and **c**) XPS spectra of C 1s and N 1s of the N-TiO_2@C nanosheets. (**d**) Time-dependent XPS spectra of N 1s of N-TiO_2@C upon Ar^+ sputtering from 0 to 960 s. (**e**) ESR spectra of the TiO_2-B and N-TiO_2@C.

The crystalline phases of the as-synthesized samples were also studied by X-ray diffraction (XRD) analysis. As shown in Figure 4a, all the identified peaks of the TiO_2-NS can be indexed to anatase TiO_2.[27] For the TiO_2-B, all the diffraction peaks can be assigned to the rutile phase of TiO_2.[19] With regard to N-TiO_2@C, an additional peak at 25.4° was detected besides the typical diffraction peaks of rutile TiO_2, which can be attributed to the (101) facet of the anatase phase of TiO_2. In addition, a weak diffraction peak at 37.8 ° was observed on N-TiO_2@C, which can be ascribed to the (111) facet of TiN (Figure S5a, b). Notably, two broad peaks with 2θ values of 25.1° and 44.2° are also observed in the XRD patterns of N-TiO_2@C (Figure 4a and Figure S5b), which can be indexed to the (002) and (101) planes of graphitic carbon,[41] respectively. This result confirms that the BA functionalized C_3N_4 nanosheets in TiO_2@C_3N_4 are indeed converted into graphitic carbon during the thermal treatment under a nitrogen atmosphere.

Based on the previous report,[42] the transformation of BA functionalized C_3N_4 nanosheets into graphitic carbon is explained as follows. Brielfly, BA was firstly functionalized on C_3N_4 nanosheets. Then, TiO_2 nanosheets were coated onto the surface of C_3N_4 nanosheets. Under thermal treatment at 1073 K in N_2, C_3N_4 nanosheets were completely decomposed as evidenced by the thermogravimetric analysis (Figure S6) while BA were condensed and crystallized into graphitic carbon during this process (Figure S7). Further insights into the structural information are obtained from Raman spectroscopy (Figure S8). The typical Raman spectrum of the TiO_2-NS exhibits five peaks at 144, 197, 395, 519 and 639 cm^{-1}, which can be

assigned to the characteristic vibrations of the anatase phase.[43] For the TiO_2-B, three Raman peaks at 226, 432 and 602 cm^{-1} agree well with a previous report for rutile TiO_2.[43] With regard to N-TiO_2@C, the Raman active modes of both rutile and anatase TiO_2 are observed from the sample. In addition, an obvious blue-shift of the peak corresponding to the E_{1g} mode of the anatase phase is observed from N-TiO_2@C as compared to TiO_2-B, attributed to nonstoichiometry caused by the existence of oxygen vacancies in the bulk of TiO_2.[44] Moreover, typical G band (~1580 cm^{-1}) and D band (~1347 cm^{-1}) features for carbon materials are observed on the N-TiO_2@C,[41] but cannot be observed from the C_3N_4 and other samples. The electronic structure of carbon in N-TiO_2@C are further studied by EELS analysis. As shown in Figure S9, the *C-K* edge for N-TiO_2@C shows two peaks at ~285 eV and ~296 eV, which are attributed to the 1s-π* transition and 1s-σ* transition in graphitic structure (Figure S9).[45] These results further confirm the transformation of C_3N_4 into graphitic carbon nanosheets during the thermal treatment process.

The chemical composition and valence state of the N-TiO_2@C nanosheets were also investigated by X-ray photoelectron spectroscopy (XPS). The quantitative analysis of N-TiO_2@C by XPS shows that the atomic ratios of Ti, O, N and C elements was determined to be 1.0 : 1.9 : 0.23 : 2.07, which is largely consistent with the EDX analysis. The C 1s spectrum of N-TiO_2@C shows four peaks at 284.6, 285.7, 287.2 and 288.7 eV (Figure 4b), assigned to C-C/C=C, C-O, C=O/C=N, and O=C-O/C-N configurations,[46] respectively. FTIR spectrum (Figure S10) further reveals the existence of functional groups such as C-H (2808, 1366 cm^{-1}), C=C/C=N

(1615, 1511 and 1453 cm^{-1}), C-N (1279 and 1024 cm^{-1}) and C-O (1140 cm^{-1}) on N-TiO_2@C,[46] in accordance with the XPS results. The N 1s peaks at 397.6 and 399.7 eV reveal that nitrogen stays at pyridinic and graphitic sites,[47] respectively (Figure 4c). These characterizations suggest that the carbon nanosheets in N-TiO_2@C are doped with nitrogen atoms as well.

The N 1s spectrum in Figure 4c also shows a distinct peak centered at 396.2 eV, attributed to Ti-N bonds. The Ti $2p_{3/2}$ peak for N-TiO_2@C can be decomposed into two sub-peaks located at 459.1 and 456.9 eV, which can be assigned to Ti-O and Ti-N bonds,[48] respectively (Figure S11). These results indicate nitrogen ions are substitutionally doped into the TiO_2 structure, fully consistent with the EELS analysis. Moreover, the nearly unchanged peak position and area of N 1s upon Ar^+ sputtering for a long time suggest the homogeneous incorporation of the nitrogen dopants in the structure of N-TiO_2@C (Figure 4d). That oxygen vacancies induced by the nitrogen ion doping are created on N-TiO_2@C to maintain electrovalence balance[49] is evidenced by the electron spin resonance (ESR) analysis (Figure 4e). In strong contrast, no oxygen vacancy signal at g=2.004 is observed on TiO_2-B without nitrogen doping.

Catalytic Activity. Liquid-phase reduction of 4-nitrophenol (4-NP), with excess $NaBH_4$ as the reductant, was carried out under controlled conditions. When no catalyst was involved, no reduction at all occurred even after prolonging the reaction time to 60 minutes (Figure S12). With the addition of N-TiO_2@C, the featured absorption peak centered at 400 nm for 4-NP decreases rapidly while two new peaks

emerged at 305 and 232 nm increase accordingly (Figure 5a), indicating the formation of 4-aminophenol (4-AP),[17, 22] further confirmed by the mass spectrometric analysis (Figure S13). Within only 10 minutes reaction time, the conversion of 4-AP reached almost 100% whereas the blank TiO_2 (TiO_2-B) and C_3N_4 nanosheets are both totally inactive for this reaction (Figure 5b). Figure 5c shows the influence of temperature on the reduction of 4-NP over the N-TiO_2@C sample. It is found that increasing temperature expedites the reduction reaction and the reactions follow pseudo-first-order kinetics. The apparent reaction rate constant deduced from the Langmuir-Hinshelwood model increased from 0.33 to 2.91 min^{-1} when increasing the reaction temperature from 298 to 328 K (Figure S14). From a linear fit to the Arrhenius plot (Inset in Figure 5c), the apparent activation energy (E_a) was calculated to be 58.1±2.9 kJ/mol, slightly larger than that for Au nanomaterials (Au nanocages: 28.1±1.4 kJ/mol; Au nanoboxes: 44.2±2.6 kJ/mol; Au hollow nanoboxes: 55.4±3.2 kJ/mol).[50]

In view of the fact that Au nanoparticles supported on TiO_2 have been intensively investigated as an excellent catalyst for the selective reduction of a wide range of nitroaromatics,[5-6, 51-53] the relative performance of N-TiO_2@C by comparison with state-of–art Au/TiO_2 catalysts fabricated by either room temperature photodeposition or high temperature calcination was also investigated. It was found that only the Au/TiO_2 sample fabricated by photo-depositing 2.0 wt% of Au onto the surface of P25 TiO_2 exhibited comparable activity to that of the N-TiO_2@C while all other samples showed far inferior activities (Figure 5b and Figure S15). More importantly,

the performance of N-TiO_2@C is rather stable during recycled long-term catalytic reactions (Figure 5d) whereas all the Au/TiO_2 catalysts prepared deactivate within only three cycles (Figure 5e). Because of the strong adsorption of the 4-AP product on the Au surface,[17] the deactivation of the Au catalyst in such a kind of reaction is unavoidable.[5, 17] In addition, the turn over number (TON) of N-TiO_2@C for the 4-NP reduction is significantly larger than 1 (See Supplementary Turnover number calculations), further confirming that the 4-NP reduction is truly driven by a catalytic process.

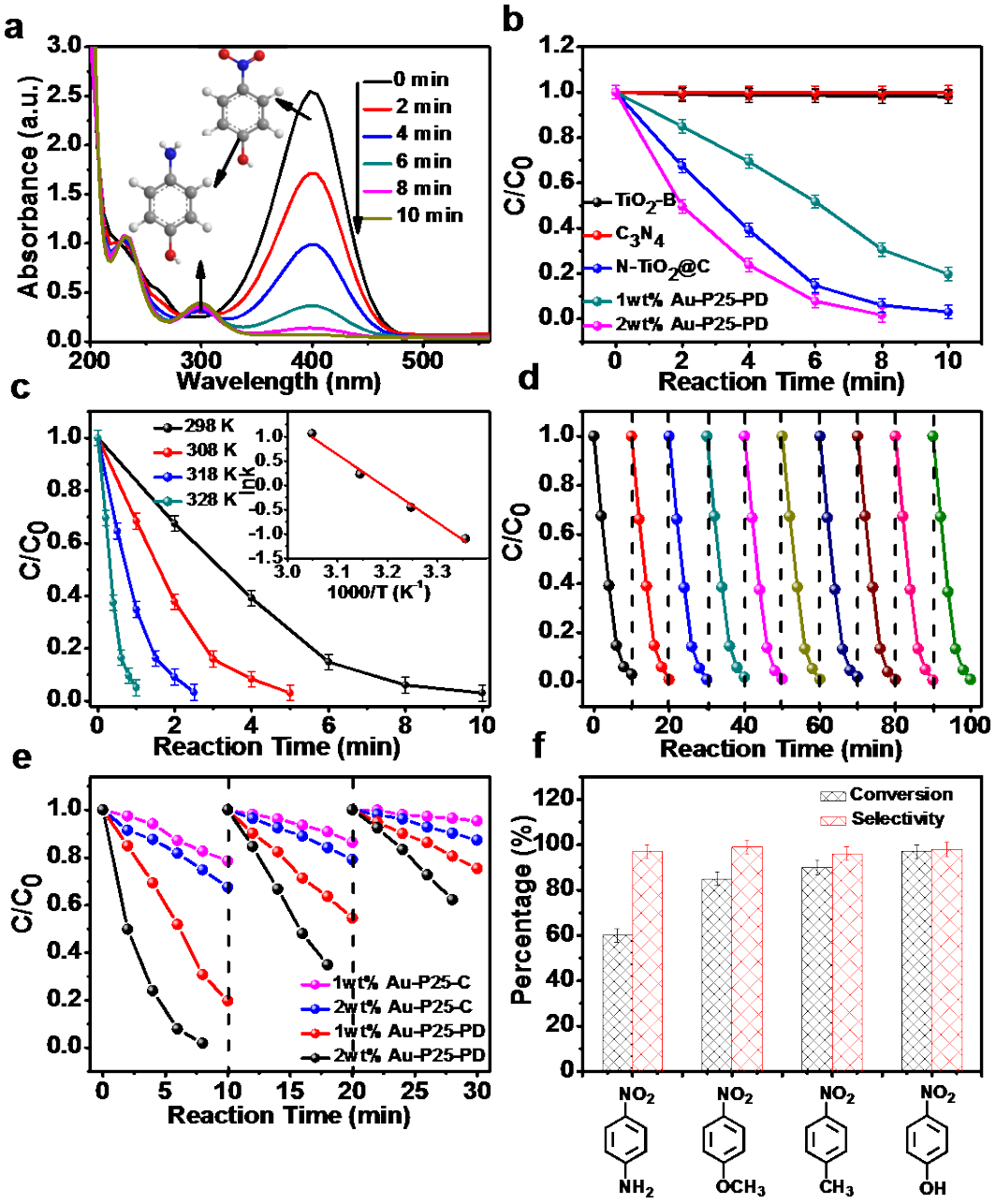

Figure 5. Catalytic reduction of nitroaromatics. (**a**) UV-visible absorption spectra recorded during the catalytic reduction of 4-nitrophenol (4-NP) over N-TiO_2@C nanosheets at 298 K. (**b**) Residual fraction of 4-NP in solution as a function of reaction time upon treatment with various catalysts. (**c**) 4-NP reduction over N-TiO_2@C at different reaction temperatures as a function of time. Inset shows the corresponding Arrhenius plot. (**d**) Recycled testing of catalytic activity of N-TiO_2@C toward 4-NP reduction at 298 K. (**e**) Recycled testing of catalytic activity of Au-TiO_2

toward 4-NP reduction at 298 K. (**f**) Conversion efficiencies for the reduction of some other substituted nitroaromatics catalyzed by N-TiO_2@C.

The selectivity of the 4-AP product by 4-NP reduction over N-TiO_2@C is determined to be ~97% (Figure S16) based on a quantitative analysis of the featured absorption peak of 4-AP, consistent with high performance liquid chromatograph analysis where a selectivity ~98% was obtained (Figure 5f). Moreover, it is found that N-TiO_2@C also exhibits excellent performance for the reduction of some other substituted nitroaromatics with a high selectivity (96~99%), although the conversion efficiency varies from 60% to 97% depending on the specific reduction reactions involved (Figure 5f).

Origin of unexpected catalytic activity. As described above, the N-TiO_2@C prepared by the C_3N_4 templating method exhibits superior performance toward the reduction of nitroaromatics while TiO_2-B synthesized by the same procedure without the C_3N_4 template is completely inactive for this reaction. It is therefore important to understand how the C_3N_4 templating method results in the remarkable properties of N-TiO_2@C. From the above results, it can be concluded that the C_3N_4 acts as a multifunctional structure-directing agent during the synthetic procedure: (I) as a 2D template for the synthesis of TiO_2 nanosheets with small particle size (3-5 nm); (II) as a phase transformation inhibitor that retards the phase transformation of TiO_2 from anatase to rutile and (III) as a source of nitrogen for doping into both TiO_2 and the carbon nanosheets.

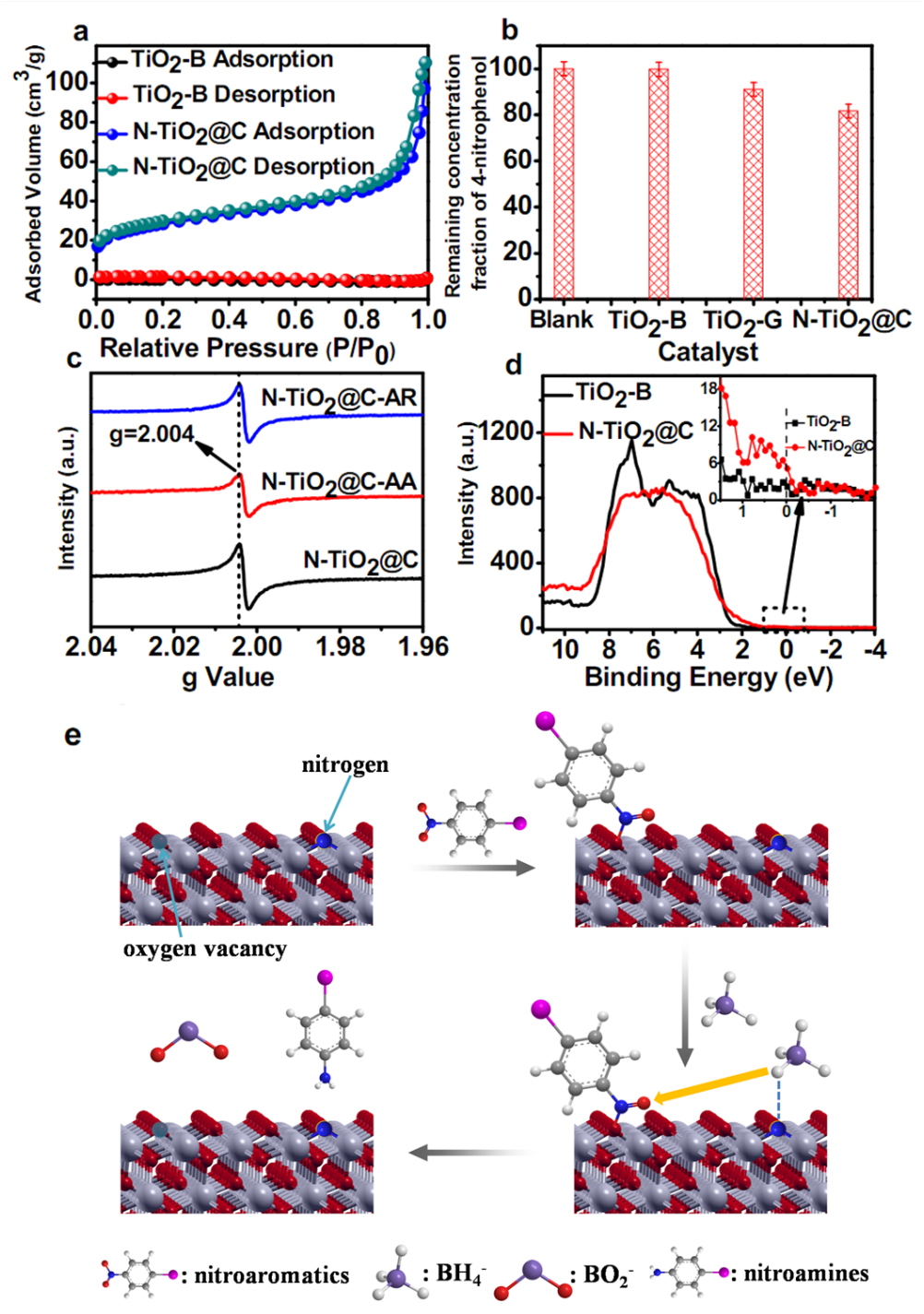

Figure 6. Origin of the catalytic performance and reaction mechanism. (**a**) The N_2 adsorption-desorption isotherms for TiO_2-B and N-TiO_2@C measured at 77 K. (**b**) Bar plots showing the remaining concentration fraction of 4-nitrophenol after the adsorption-desorption equilibrium in the dark over the TiO_2-B, TiO_2-G and N-TiO_2@C catalysts, respectively. (**c**) ESR spectra of N-TiO_2@C before adsorbing

4-NP, N-TiO_2@C after adsorbing 4-NP (TiO_2-AA) and N-TiO_2@C after the reduction reaction (TiO_2-AR). (**d**) XPS spectra of N-TiO_2@C and TiO_2-B showing the valence bands close to the Fermi level. (**e**) Proposed reaction mechanism of nitroaromatic reduction over N-TiO_2@C (carbon atoms were omitted in the model for simplicity).

To understand the influence of these factors on the performance of N-TiO_2@C, a variety of controlled experiments were carried out. Firstly, the influence of C_3N_4 as a 2D template on the surface area and porosity of the TiO_2 samples is studied by nitrogen adsorption-desorption measurements (Figure 6a). The blank TiO_2 (TiO_2-B) shows a type II isotherm with a small surface area of 0.2 m^2/g, which indicates a nonporous structure. The N-TiO_2@C composite nanosheets show reversible type IV isotherms with a much larger surface area of 99 m^2/g, indicating the presence of mesopores (Figure S17). Such a porous 2D structure of N-TiO_2@C with an enhanced surface area and small particle size (3-5 nm) would facilitate the adsorption of the reactants (Figure 6b). Nevertheless, the enhanced adsorption capacity of N-TiO_2@C on its own cannot account for activating TiO_2 for nitro reduction when considering the fact that the TiO_2-G nanosheets prepared by using graphene as a 2D template also show a porous 2D structure (Table S2) as well as improved adsorption ability as compared to TiO_2-B (Figure 6b) but still cannot induce the reduction of 4-NP (Figure S18).

Secondly, we also examined the possible influence of phase composition on the activity of the N-TiO_2@C catalyst. From XRD analysis (Figure 4a), it is known that the phase composition of the N-TiO_2@C is a mixture of anatase and rutile phases

while TiO_2-B consists of only the rutile phase. Therefore, questions naturally come to mind. Is the anatase phase or the mixed anatase/rutile phases of TiO_2 responsible for the unexpected catalytic activity of N-TiO_2@C? To examine this possibility, the activities of 4-NP reduction over both P25 (TiO_2) and homemade anatase TiO_2 (TiO_2-A) were measured. It is found that neither of the samples showed any activity for 4-NP reduction (Figure S15), suggesting that the phase composition of TiO_2 is not important for the catalytic activity of N-TiO_2@C.

Thirdly, to understand the unexpected catalytic performance of N-TiO_2@C, we next focused on the nitrogen dopants and the associated oxygen vacancies in the TiO_2 structure. A controlled experiment shows that activity is observed on the TiO_2 nanosheets (TiO_2-NS) having both nitrogen dopants and oxygen vacancies (Figure S19). However, neither the commercial TiN nanoparticles nor the defective TiO_2-G nanosheets with only oxygen vacancies (i.e. without nitrogen dopants) show any catalytic activity for 4-NP reduction (Figure S20). These results suggest that the oxygen vacancies and substituted nitrogen dopants have a synergistic effect on activating the TiO_2 for 4-NP reduction.

Finally, we also found that the nitrogen doped, graphitic carbon is active for 4-NP reduction while the graphitic carbon without nitrogen doping shows no catalytic activity (Figure S21). The origin of the efficient catalytic performance of N-TiO_2@C should thus be attributed to the presence of substituting nitrogen dopants and associated oxygen vacancy defects in the N-TiO_2@C nanosheets. The porous 2D structure and small particle size (3-5 nm) of N-doped TiO_2 of N-TiO_2@C further

facilitate the adsorption of the reactants and provides more active sites for catalytic reactions.

Catalytic mechanism. The above investigations have indicated that both nitrogen dopants and associated oxygen vacancy defects in the N-TiO_2@C nanosheets are critical for the remarkable activity in the nitro reduction reaction. However, it is still unclear how these species take part in the catalytic reaction. To address this issue, electron spin resonance (ESR) was further employed to probe the reaction processes. As shown in Figure 6c, the decreased concentration of single-electron-trapped oxygen vacancies in N-TiO_2@C after adsorbing 4-NP indicates that the oxygen vacancy sites participate in the adsorption of 4-NP. In view of the fact that oxygen vacancy sites are able to capture and activate the oxygen of $–NO_x$ groups,[54] it is reasonable to suggest that oxygen vacancy sites would act as trap centers for both capturing the oxygen end of the nitroaromatics as well as activating the nitro groups for subsequent reduction. Notably, the concentration of single-electron-trapped oxygen vacancies on N-TiO_2@C returns to its initial value after the catalytic reaction, indicating that the BH_4^- ions do help to release the trapped oxygen atoms from N-TiO_2@C.

Since the TiO_2-G nanosheets with oxygen vacancies only and no nitrogen dopants (TiO_2-G-OV) show no activity for 4-NP reduction, it is proposed that the hydrogenation process of the nitro groups in the presence of $NaBH_4$ occurs with the aid of the nitrogen dopants. Considering previous mechanistic studies indicate that the reduction of adsorbed nitro compounds by BH_4^- ions is mediated by the loaded metal nanoparticles,[17, 22] we speculate that a metal-like active site may exist in the

N-TiO_2@C catalyst, which is probably related to the nitrogen dopant ions. In order to examine this, the valence-band spectrum of N-TiO_2@C is collected. As shown in Figure 6d, besides the large emission from 3 to 8 eV corresponding to the O 2p valence electrons, a smaller hump at the Fermi level corresponding to the metallic feature of the sample is also in evidence.[55] This is commonly ascribed to the low-valent transition metal oxide or metal nitride.[55] Notably, this metallic feature cannot be observed on TiO_2-B without nitrogen dopants. Therefore, this feature is ascribed to Ti-N species in the nitrogen doped TiO_2 in view of the fact that TiN is a metallic compound with excellent electronic conductivity.[56] These metallic Ti-N species can interact with the BH_4^- ions via hydrogen bonding and then facilitate the hydrogenation of the nitro groups.

Notably, the TiN itself can not drive the nitro reduction reaction, as demonstrated in Figure S20. This is because of the fact that the rate-determining step for nitro reduction is the reduction of nitro group rather than the interaction of BH_4^- ions with the metal surface.[22] Due to the high bonding energy of nitro group (466 kJ/mol), its adsorption and activation are prerequisite steps for its reduction. Fortunately, this process can be achieved on the oxygen vacancy sites on TiO_2.[19] However, there is no such sites on TiN for nitro group activation. Therefore, the TiN nanoparticles show no activity for nitro reduction.

Based on the above understanding, a possible mechanism is proposed to account for the nitro reduction on the N-TiO_2@C catalyst (Figure 6e and Scheme S1): Firstly, the $–NO_2$ group of the nitroaromatics is trapped at the oxygen vacancy sites of TiO_2.

Simultaneously, the BH_4^- ions interact with the nitrogen dopants through hydrogen bonding to form a metastable iminoborohydride species. The hydride ions of these species would then be captured by the trapped oxygen atoms of the nitroaromatics, resulting in the recovering of the oxygen vacancy sites and the formation of aromatic amines.

Conclusion.

In conclusion, nitrogen doped TiO_2@carbon composite nanosheets (N-TiO_2@C) were prepared by a facile sol-gel method using C_3N_4 as a multifunctional 2D template. During the synthesis procedure, C_3N_4 not only acts as a structure-directing agent to control the shape, size and crystal phase of TiO_2 but also facilitates nitrogen doping and oxygen vacancy creation in the resultant 2D porous N-TiO_2@C nanosheets. As a result, the N-TiO_2@C composite nanosheets exhibit unexpected, highly efficient catalytic activity for selective nitro reduction at room temperature. This work provides critical insights as well as helpful guidelines for the design of low-cost but highly efficient catalysts for selective nitroaromatic reduction.

Experimental Section.

Materials. Tetrabutyl titanate (TBT), benzyl alcohol, urea, titanium nitride and anhydrous ethanol (EtOH), were purchased from Sinopharm chemical regent Co., Ltd. (Shanghai, China). Deionized water was supplied from local sources. All of the materials were used as received without further purification.

Synthesis. C_3N_4 nanosheets were obtained according to our previous report[57]. For the synthesis of nitrogen doped TiO_2@carbon nanosheets (N-TiO_2@C), C_3N_4

nanosheets were dispersed in ethanol with the aid of ultrasonication. Then benzyl alcohol and H_2O were added into the suspension followed by stirring for 1 h at 273 K. Subsequently, TBT was slowly dropped into the above suspension until the final molar ratio of a mixture of TBT: BA: EtOH : H_2O = 1 : 5 : 100 : 5 was achieved. After 2 h of stirring, the precipitation was vacuum-filtered, washed with ethanol and dried in air at room temperature. Finally, the (TiO_2@C_3N_4) product was calcined at 1073 K under a N_2 atmosphere for 4 h. Blank TiO_2 (TiO_2-B) was prepared by using the same procedure for TiO_2 nanosheets without adding the C_3N_4 template. TiO_2 nanosheets (TiO_2-NS) were obtained by calcining the TiO_2@C_3N_4 sample at 723 K under an O_2 atmosphere for 2 h.

Characterization. Crystal structures of the as-prepared samples were analyzed on a Rigaku Miniflex II X-ray powder diffractometer using Cu K_α radiation. A field-emission scanning electron microscope (FESEM, JSM-6700F) and transmission electron microscope (JEM-2010, FEI, Tecnai G^2 F20 FEG TEM) were used to identify the morphology and microscopic structure of the as-synthesized samples. High-angle annular dark-field (HAADF) imaging and electron-energy loss spectroscopy (EELS) analyses were carried out in a dedicated scanning transmission electron microscope (Nion UltraSTEM100) operated at 100 keV. The microscope is equipped with a cold field-emission gun and a corrector of third- and fifth-order aberrations for sub-angstrom resolution. The Fourier transform infrared spectroscopy (FTIR) data were collected using a VERTEX 70 spectrophotometer at a resolution of 4 cm^{-1}. X-ray photoelectron spectroscopy (XPS) measurements were performed using

a Thermo Scientific ESCA Lab250 spectrometer consisting of monochromatic Al K_α as the X-ray source, a hemispherical analyzer and a sample stage with multi-axial adjustability to obtain the composition on the surface of samples. All the binding energies were calibrated by the C 1s peak of the surface adventitious carbon at 284.6 eV. The Brunauer-Emmett-Teller (BET) specific surface areas of the samples were measured by a TriStar II 3020-BET/BJH Surface Area analyzer. Raman spectra were collected using a FLS920 spectrometer. Electron spin resonance (ESR) studies were carried out on an ELEXSYS E500 spectrometer equipped with a nitrogen cryostat. All the spectra were collected at 100 K.

Catalytic Activities. The catalytic nitro reduction was carried out in a beaker. Typically, 20 mg of $NaBH_4$ was added into 60 mL of aqueous nitroaromatic solution (20 mg/L). The mixture was then stirred in the dark for 5 min to generate a uniform aqueous solution. Subsequently, 10 mg of the catalyst was added into the above solution. During the reaction, 2 mL of solution was sampled by a syringe and filtered using a 0.45 um Millpore film at each time interval for UV-visible absorption spectroscopy analysis. The conversion and selectivity of the reaction were determined by quantitative analysis of the featured absorption peaks centered at ~400 and ~232 nm for 4-nitrophenol and 4-aminophenol, respectively, and also examined with high performance liquid chromatography (waters-600). The mass spectrometry data was performed on a Bruker Impact II MS. The catalysts after reaction were washed with distilled water carefully and then dried in an oven at 353 K overnight for the following cycling activity test.

ASSOCIATED CONTENT

Supporting information. The SEM, TEM images, Raman, FTIR, XPS spectra and ESR spectra of the samples; This material is available free of charge via the Internet at http://pubs.acs.org.

AUTHOR INFORMATION

Corresponding Author
* Prof. Zhiguo Yi Email: zhiguo@fjirsm.ac.cn

Notes
The authors declare no competing financial interest.

ACKNOWLEDGMENT

This work was financially supported by the National Key Project on Basic Research (Grant No. 2013CB933203), the Strategic Priority Research Program of the Chinese Academy of Sciences (Grant No. XDB20000000), the Natural Science Foundation of China (Grants No. 21607153, 21373224 and 21577143), the Natural Science Foundation of Fujian Province (Grant No. 2015J05044), and the Frontier Science Key Project of the Chinese Academy of Sciences (QYZDB-SSW-JSC027). The work at ORNL was supported by the U.S. Department of Energy, Office of Science, Basic Energy Sciences, Materials Science and Engineering Division (STEM-EELS) and through a user project supported by ORNL's Center for Nanophase Materials Sciences, which is sponsored by the Scientific User Facilities Division of U.S. DOE.**REFERENCES.**

1. Tafesh, A. M.; Weiguny, J. *Chem. Rev.* 1996, 96, 2035-2052.

2. Downing, R. S.; Kunkeler, P. J.; van Bekkum, H. *Catal. Today* 1997, 37, 121-136.

3. Wolfe, J. P.; Wagaw, S.; Marcoux, J.-F.; Buchwald, S. L. *Acc. Chem. Res.* 1998, 31, 805-818.

4. Stephen, A. Amines: Synthesis, Properties and Applications. Cambridge University Press: 2006.

5. Corma, A.; Serna, P. *Science* 2006, 313, 332-334.

6. Blaser, H.-U.; Steiner, H.; Studer, M. *Chem. Cat. Chem.* 2009, 1, 210-221.

7. Wei, H.; Liu, X.; Wang, A.; Zhang, L.; Qiao, B.; Yang, X.; Huang, Y.; Miao, S.; Liu, J.; Zhang, T. *Nat. Commun.* 2014, 5, 5634.

8. Vilé, G.; Almora-Barrios, N.; López, N.; Pérez-Ramírez, J. *ACS Catal.* 2015, 5, 3767-3778.

9. Feng, J.; Handa, S.; Gallou, F.; Lipshutz, B. H. *Angew. Chem., Int. Ed.* 2016, 55, 8979-8983.

10. Hakki, A.; Dillert, R.; Bahnemann, D. W. *Phys. Chem. Chem. Phys.* 2013, 15, 2992-3002.

11. Ismail, A. A.; Hakki, A.; Bahnemann, D. W. *J. Mol. Catal. A: Chem.* 2012, 358, 145-151.

12. Hakki, A.; Dillert, R.; Bahnemann, D. *Catal. Today* 2009, 144, 154-159.

13. Suchy, M.; Winternitz, P.; Zeller, M. *Catal. Today* 1997, 37, 121-136.

14. Blaser, H.; Siegrist, U.; Steiner, H.; Studer, M.; Sheldon, R.; van Bekkum, H. *Weinheim: Wiley/VCH* 2001, 389.

15. Ahn, W.-Y.; Sheeley, S. A.; Rajh, T.; Cropek, D. M. *Appl. Catal., B* 2007, 74, 103-110.

16. Imamura, K.; Iwasaki, S.-i.; Maeda, T.; Hashimoto, K.; Ohtani, B.; Kominami, H. *Phys. Chem. Chem. Phys.* 2011, 13, 5114-5119.

17. Lin, F.-h.; Doong, R.-a. *J. Phys. Chem. C* 2011, 115, 6591-6598.

18. Wang, X.; Liu, D.; Song, S.; Zhang, H. *J. Am. Chem. Soc.* 2013, 135, 15864-15872.

19. Shiraishi, Y.; Hirakawa, H.; Togawa, Y.; Sugano, Y.; Ichikawa, S.; Hirai, T. *ACS Catal.* 2013, 3, 2318-2326.

20. Shukla, A.; Singha, R. K.; Sasaki, T.; Bal, R. *Green Chem.* 2015, 17, 785-790.

21. Zhang, S.; Chang, C.-R.; Huang, Z.-Q.; Li, J.; Wu, Z.; Ma, Y.; Zhang, Z.; Wang, Y.; Qu, Y., *J. Am. Chem. Soc.* 2016, 138, 2629-2637.

22. Wunder, S.; Polzer, F.; Lu, Y.; Mei, Y.; Ballauff, M. *J. Phys. Chem. C* 2010, 114, 8814-8820.

23. Su, Y.; Lang, J.; Li, L.; Guan, K.; Du, C.; Peng, L.; Han, D.; Wang, X. *J. Am. Chem. Soc.* 2013, 135, 11433-11436.

24. Kong, X.-k.; Sun, Z.-y.; Chen, M.; Chen, C.-l.; Chen, Q.-w. *Energy Environ. Sci.* 2013, 6, 3260-3266.

25. Hoffmann, M. R.; Martin, S. T.; Choi, W.; Bahnemann, D. W. *Chem. Rev.* 1995, 95, 69-96.

26. Fujishima, A.; Zhang, X. *C. R. Chim.* 2006, 9, 750-760.

27. Pan, X.; Yang, M.-Q.; Tang, Z.-R.; Xu, Y.-J. *J. Phys. Chem. C* 2014, 118, 27325-27335.

28. Boronat, M.; Concepción, P.; Corma, A.; González, S.; Illas, F.; Serna, P. *J. Am. Chem. Soc.* 2007, 129, 16230-16237.

29. Corma, A.; Serna, P.; Concepción, P.; Calvino, J. J. *J. Am. Chem. Soc.* 2008, 130, 8748-8753.

30. Asahi, R.; Morikawa, T.; Ohwaki, T.; Aoki, K.; Taga, Y. *Science* 2001, 293, 269-271.

31. Jagadeesh, R. V.; Surkus, A.-E.; Junge, H.; Pohl, M.-M.; Radnik, J.; Rabeah, J.; Huan, H.; Schünemann, V.; Brückner, A.; Beller, M. *Science* 2013, 342, 1073-1076.

32. Naik, G. V.; Shalaev, V. M.; Boltasseva, A. *Adv. Mater.* 2013, 25, 3264-3294.

33. Asahi, R.; Morikawa, T.; Irie, H.; Ohwaki, T. *Chem. Rev.* 2014, 114, 9824-9852.

34. Lin, T.; Chen, I.-W.; Liu, F.; Yang, C.; Bi, H.; Xu, F.; Huang, F. *Science* 2015, 350, 1508-1513.

35. Huang, X.; Zhao, Z.; Cao, L.; Chen, Y.; Zhu, E.; Lin, Z.; Li, M.; Yan, A.; Zettl, A.; Wang, Y. M.; Duan, X.; Mueller, T.; Huang, Y. *Science* 2015, 348, 1230-1234.

36. Yang, S.; Gong, Y.; Zhang, J.; Zhan, L.; Ma, L.; Fang, Z.; Vajtai, R.; Wang, X.; Ajayan, P. M. *Adv. Mater.* 2013, 25, 2452-2456.

37. Sun, Z.; Liao, T.; Dou, Y.; Hwang, S. M.; Park, M.-S.; Jiang, L.; Kim, J. H.; Dou, S. X. *Nat. Commun.* 2014, 5, 3813.

38. Deng, D.; Novoselov, K. S.; Fu, Q.; Zheng, N.; Tian, Z.; Bao, X. *Nat. Nanotech.* 2016, 11, 218-230.

39. Wang, X.; Maeda, K.; Thomas, A.; Takanabe, K.; Xin, G.; Carlsson, J. M.; Domen, K.; Antonietti, M. *Nat. Mater.* 2009, 8, 76-80.

40. Stoyanov, E.; Langenhorst, F.; Steinle-Neumann, G.,*Am. Mineral.* 2007, 92, 577-586.

41. Pachfule, P.; Shinde, D.; Majumder, M.; Xu, Q. *Nat. Chem.* 2016, 8, 718-724.

42. Yu, H.; Shang, L.; Bian, T.; Shi, R.; Waterhouse, G. I. N.; Zhao, Y.; Zhou, C.; Wu, L.-Z.; Tung, C.-H.; Zhang, T. *Adv. Mater.* 2016, 28, 5080-5086.

43. Yin, H.; Wada, Y.; Kitamura, T.; Kambe, S.; Murasawa, S.; Mori, H.; Sakata, T.; Yanagida, S. *J. Mater. Chem.* 2001, 11, 1694-1703.

44. Eder, D.; Windle, A. H. *Adv. Mater.* 2008, 20, 1787-1793.

45. Glerup, M.; Castignolles, M.; Holzinger, M.; Hug, G.; Loiseau, A.; Bernier, P. *Chem. Commun.* 2003, 2542-2543.

46. Yang, P.; Zhao, J.; Wang, J.; Cui, H.; Li, L.; Zhu, Z. *ChemPhysChem* 2015, 16, 3058-3063.

47. Gao, Y.; Hu, G.; Zhong, J.; Shi, Z.; Zhu, Y.; Su, D. S.; Wang, J.; Bao, X.; Ma, D. *Angew. Chem., Int. Ed.* 2013, 52, 2109-2113.

48. Liu, G.; Wang, L.; Sun, C.; Yan, X.; Wang, X.; Chen, Z.; Smith, S. C.; Cheng, H.-M.; Lu, G. Q. *Chem. Mater.* 2009, 21, 1266-1274.

49. Wang, J.; Tafen, D. N.; Lewis, J. P.; Hong, Z.; Manivannan, A.; Zhi, M.; Li, M.; Wu, N. *J. Am. Chem. Soc.* 2009, 131, 12290-12297.

50. Zeng, J.; Zhang, Q.; Chen, J.; Xia, Y. *Nano Lett.* 2010, 10, 30-35.

51. Mitsudome, T.; Kaneda, K. *Green Chem.* 2013, 15, 2636-2654.

52. Zhao, P.; Feng, X.; Huang, D.; Yang, G.; Astruc, D. *Coord. Chem. Rev.* 2015, 287, 114-136.

53. Takale, B. S.; Bao, M.; Yamamoto, Y. *Org. Biomol. Chem.* 2014, 12, 2005-2027.

54. Wu, Q.; van de Krol, R. *J. Am. Chem. Soc.* 2012, 134, 9369-9375.

55. Vettraino, M.; Trudeau, M.; Lo, A. Y. H.; Schurko, R. W.; Antonelli, D. *J. Am. Chem. Soc.* 2002, 124, 9567-9573.

56. Saha, N. C.; Tompkins, H. G. *J. Appl. Phys.* 1992, 72, 3072-3079.

57. Chen , X.; Huang, X.; Yi, Z. *Chem. Eur. J.* 2014, 20, 17590-17596.

For Table of Contents Only

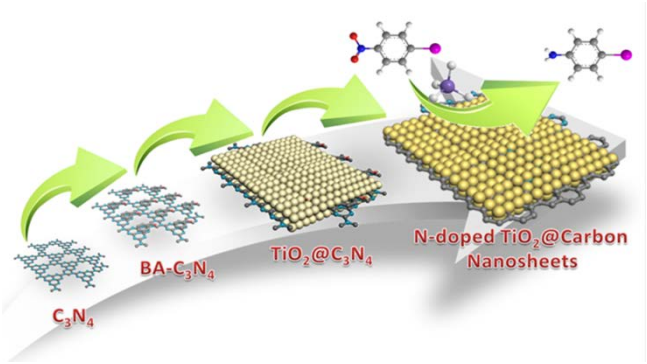

Supporting Information

Design Synthesis of Nitrogen-Doped TiO_2@Carbon Nanosheets toward Selective Nitroaromatics Reduction under Mild Conditions

Xiaoyang Pan[1], Xiang Gao[2], Xuxing Chen[1], Ho Nyung Lee[2], Yun Liu[3], Ray L. Withers[3] and Zhiguo Yi[*1,4]

[1]CAS Key Laboratory of Design and Assembly of Functional Nanostructures & Fujian Provincial Key Laboratory of Nanomaterials, Fujian Institute of Research on the Structure of Matter, Chinese Academy of Sciences, Fuzhou 350002, China.

[2]Materials Science and Technology Division, Oak Ridge National Laboratory, Oak Ridge, TN 37831, USA

[3]Research School of Chemistry, The Australian National University, ACT 2601, Australia

[4]University of Chinese Academy of Sciences, Beijing 100049, China

The Supporting Info includes:

Figures S1-21

Turnover number calculation

Tables S1 and S2

Scheme S1

[*] Email: zhiguo@fjirsm.ac.cn

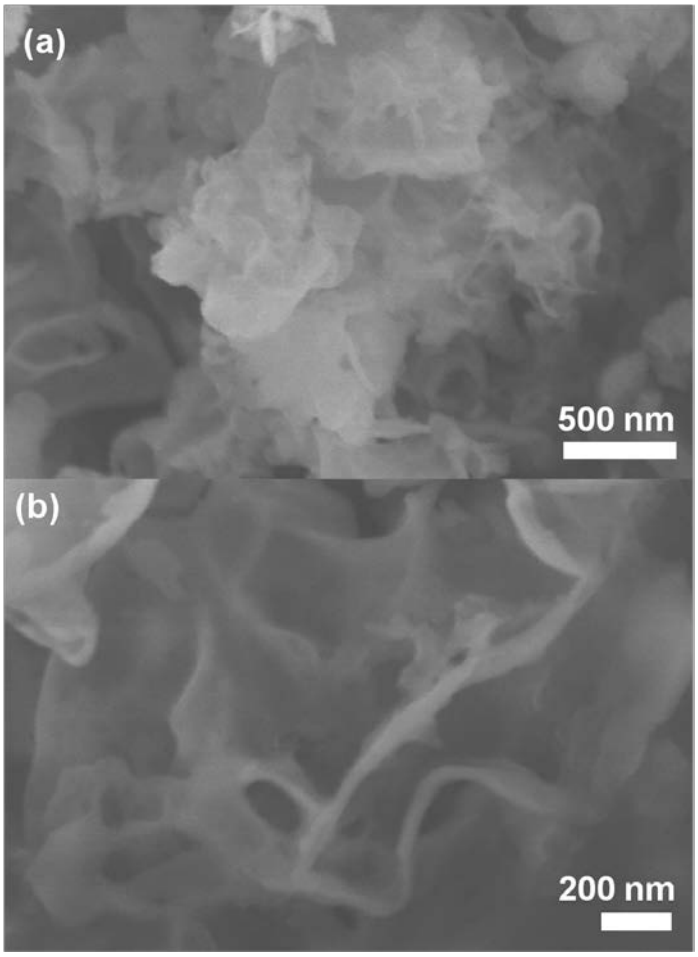

Figure S1. SEM images (a, b) of C_3N_4 nanosheets.

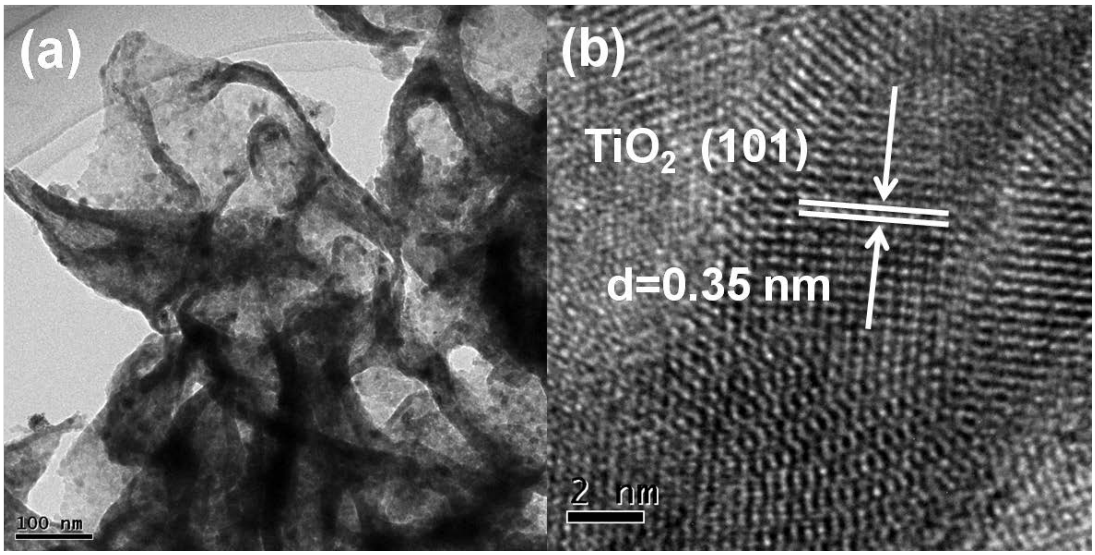

Figure S2. The TEM (a), HRTEM (b) images of the TiO_2 nanosheets (TiO_2-NS).

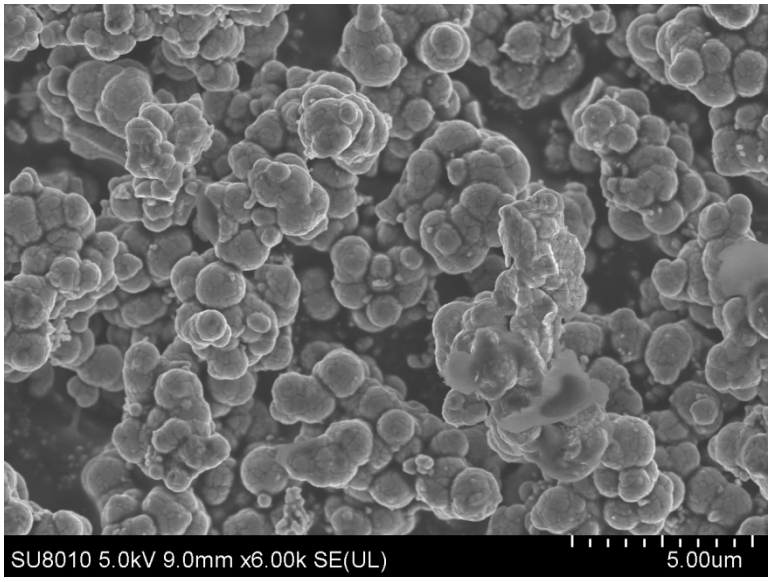

Figure S3. The SEM image of blank TiO_2 (TiO_2-B) prepared using the same procedure as that for nitrogen doped TiO_2@carbon nanosheets (N-TiO_2@C) but without adding C_3N_4 template.

Table S1. The weight and atomic ratios of C, N, O and Ti elements in the nitrogen doped TiO_2@carbon (N-TiO_2@C) nanosheets.

Element	Weight (%)	Atomic (%)
C	24.76	42.81
N	2.59	3.84
O	25.28	32.81
Ti	47.37	20.54

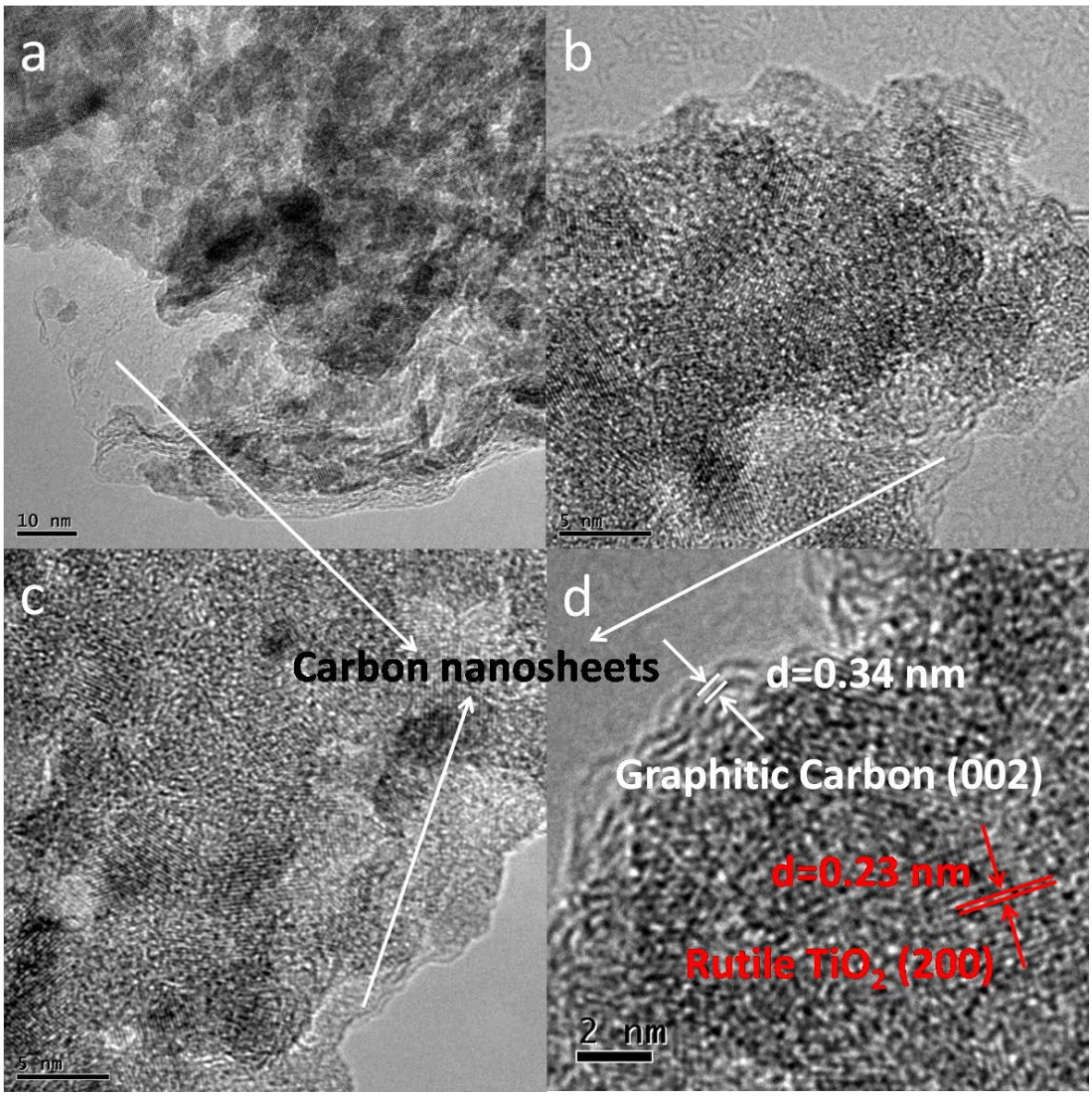

Figure S4. Additional TEM images of the N-TiO_2@C.

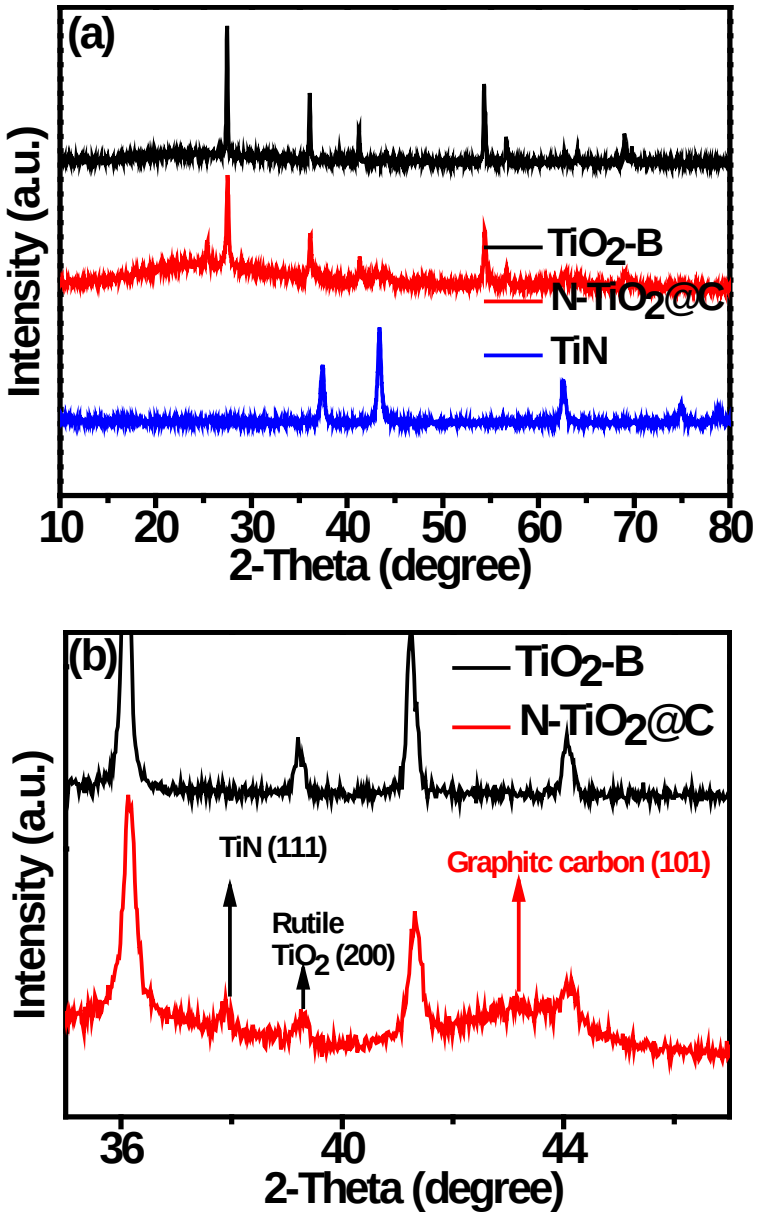

Figure S5. (a) XRD patterns of the TiO_2-B, N-TiO_2@C and TiN. (b) Enlarged XRD patterns of TiO_2-B and N-TiO_2@C.

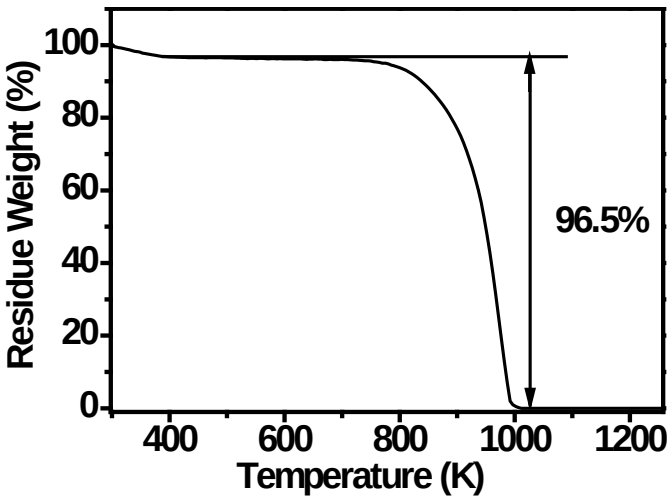

Figure S6. Thermogravimetric (TGA) analysis of C_3N_4. in N_2 with a temperature rise rate of 5 K/min.

Note: The weight loss (3.5) prior to 373 K was due to the desorption of the water. The weight loss (96.5%) after 373 K was due to the decomposition of C_3N_4.

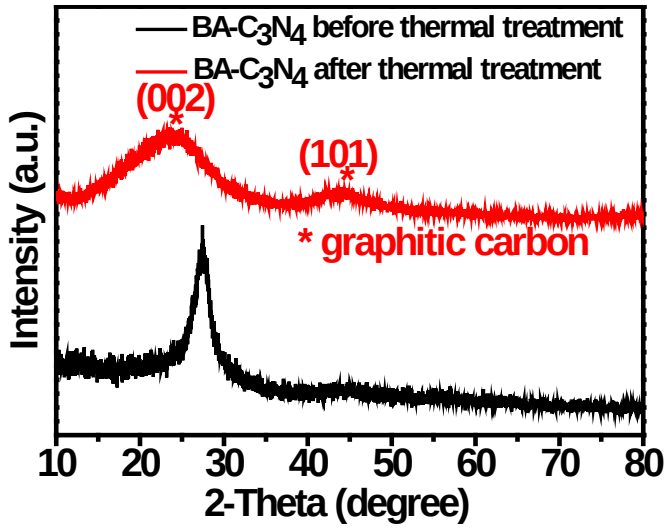

Figure S7. The XRD patterns of BA-functionalized C_3N_4 nanosheets (BA- C_3N_4) before and after treated at 1073 K for 2h in N_2.

Note: The typical XRD peak of g-C_3N_4 at 27° is disappeared while the typical XRD patterns of graphitic carbon are appeared after the thermal treatment. These results suggest that the C_3N_4 nanosheets are decomposed and BA on C_3N_4 surface is transformed into graphitic carbon.

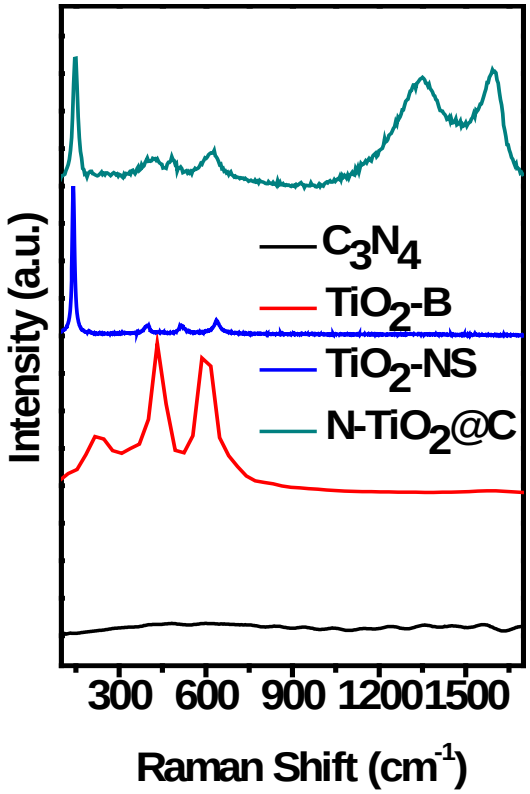

Figure S8. The Raman spectra of the C_3N_4, blank TiO_2 (TiO_2-B), TiO_2 nanosheets (TiO_2-NS) and nitrogen doped TiO_2@carbon nanosheets (N-TiO_2@C).

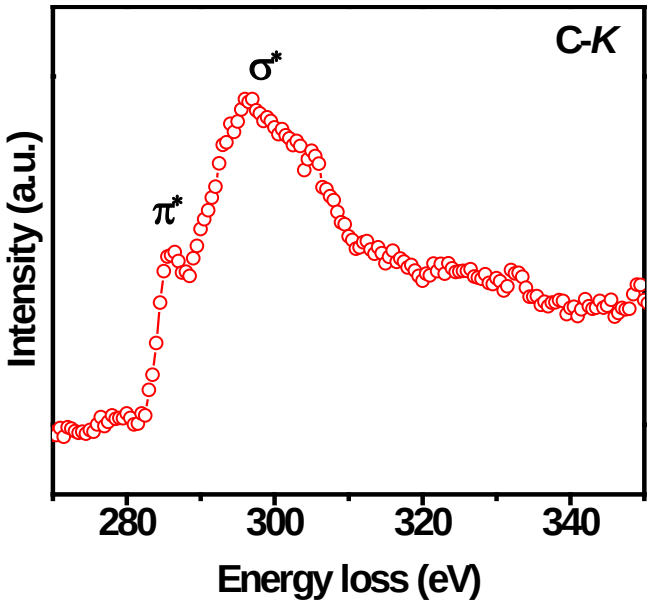

Figure S9. The EELS spectrum of the C-*K* edge of N-TiO_2@C.

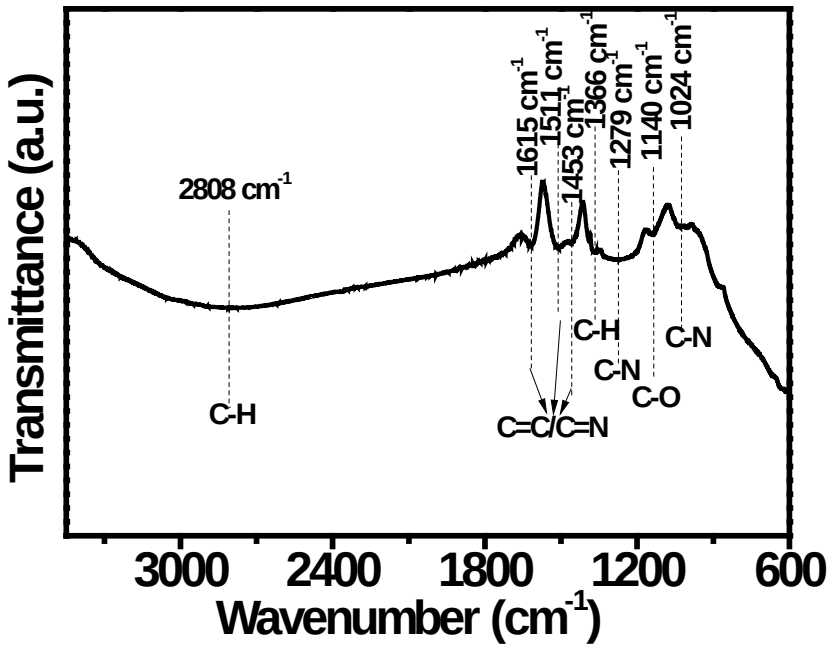

Figure S10. The FTIR spectrum of the nitrogen doped TiO_2@carbon nanosheets (N-TiO_2@C).

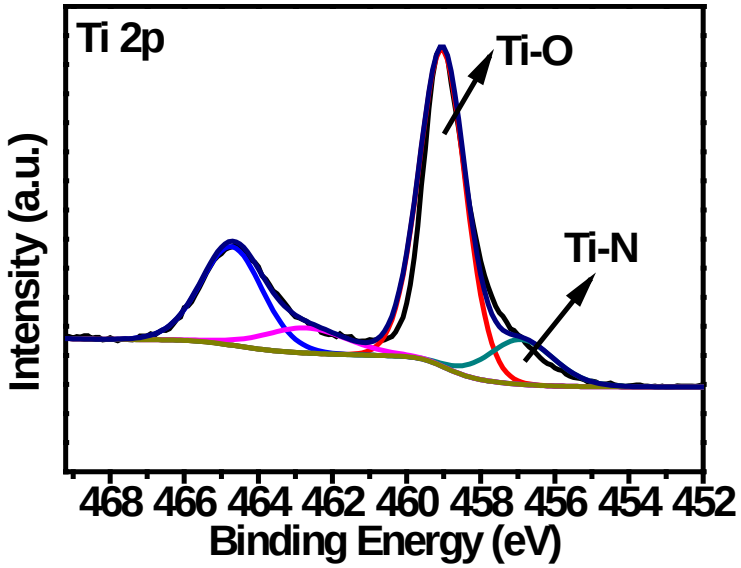

Figure S11. The XPS spectrum of Ti 2p for the N-TiO_2@C.

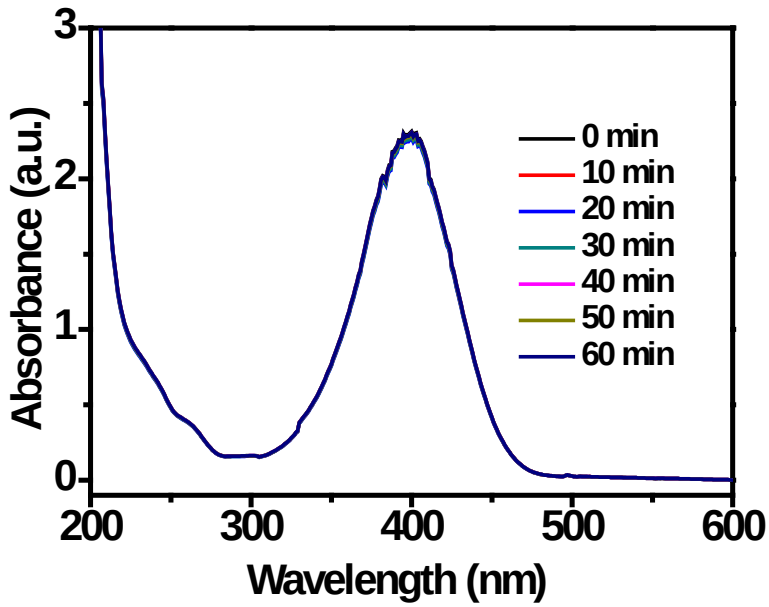

Figure S12. UV-visible absorption spectra recorded during the catalytic reduction of 4-nitrophenol without catalyst at 298 K.

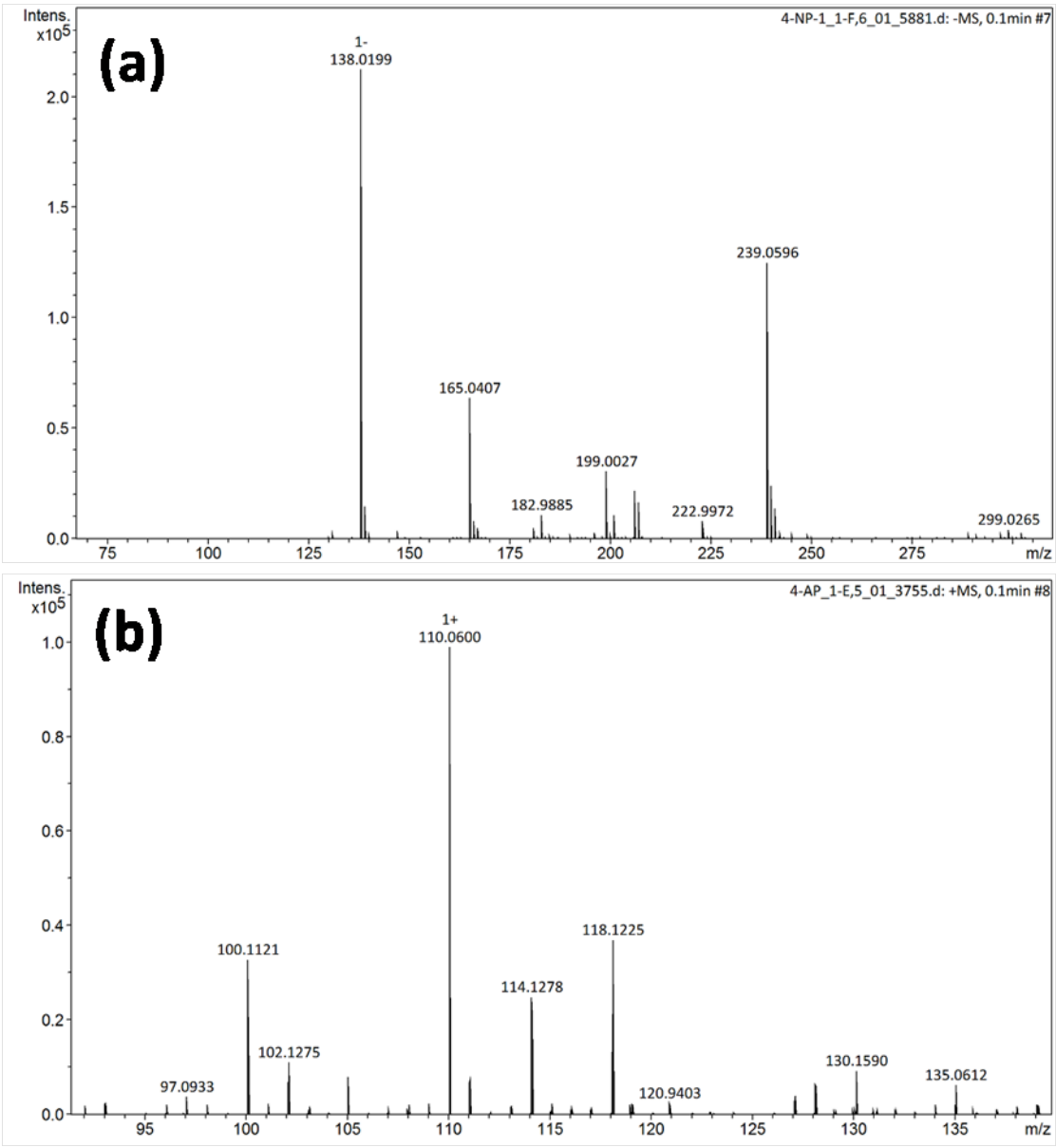

Figure S13. Mass spectrogram of the reaction solution. (a) the 4-nitrophenol solution at a reaction time of t=0 min. (b) The final reduction product at a reaction time of t=10 min.

Note: As shown in **Figure S9a**, the mass peak at 138.0199 is assigned for 4-nitrophenol anion. The mass peak at 110.0600 is assigned for protonated 4-aminophenol (**Figure S9b**).

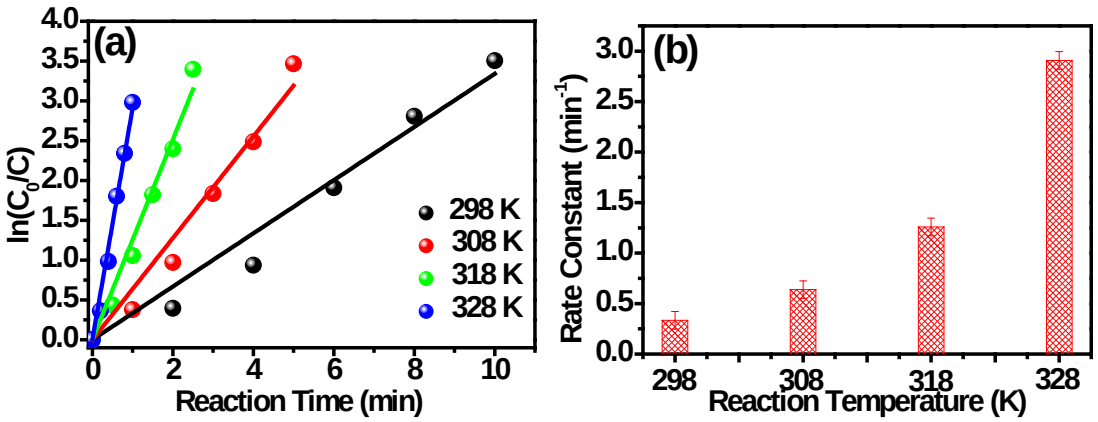

Figure S14. Catalytic reduction of 4-nitrophenol over N-TiO_2@C at different temperatures. (a) The kinetic rate constant curves. (b) The apparent rate constants.

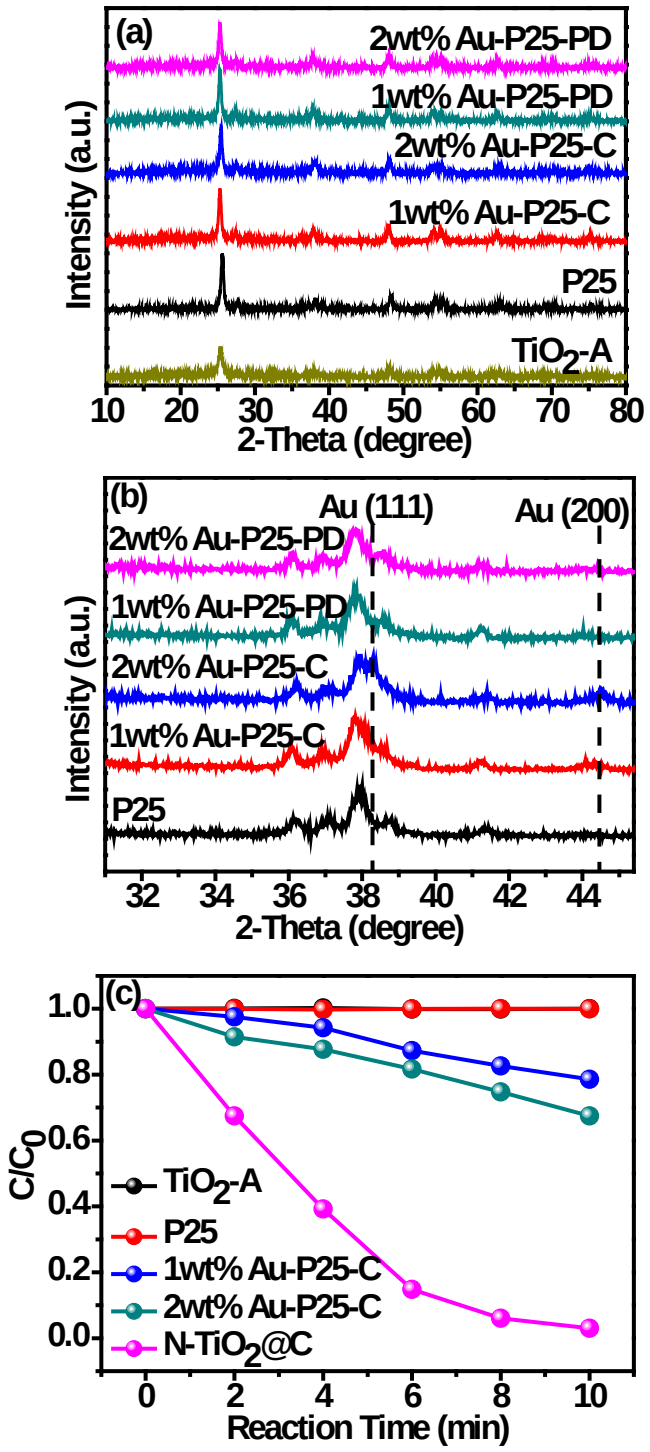

Figure S15. XRD and catalytic properties of the as-prepared samples. (a) The XRD patterns of P25, Au-P25-C, Au-P25-PD and TiO_2-A. (b) Enlarged XRD patterns of the P25, Au-P25-C and Au-P25-PD in the range of 30-46 degree. (c) Residual fraction of 4-nitrophenol in solution as a function of reaction time upon treatment with various catalysts.

Note: The Au-P25-C samples were prepared as follows: 0.1 g P25 was dispersed in 50 ml H_2O. Then, a certain amount of $HAuCl_4$ (5mM) solution was added into the suspension. Subsequently, the suspension was heated at 353 K to remove water. After that, the as-obtained powders were further dried in an oven at 373 K overnight. Then, the powders were calcined at 673 K for 2 hours. The Au-P25-PD samples were prepared as follows: 0.1 g P25 was dispersed in 30 ml H_2O. Then, 20 ml ethanol was added into the suspension. Subsequently, a certain amount of $HAuCl_4$ (5 mM) solution was added into the suspension. The suspension was irradiated with UV light (365 nm) by a Xe lamp for 2 hours. After that, the as-obtained powders were further dried in an oven at 373 K overnight. Anatase TiO_2 (TiO_2-A) was prepared as follows: 1.7 mL TBOT was slowly added into 100 mL ethanol which contained 0.45 mL H_2O. Then, the suspension was stirred at room temperature for 10 hours. After that, the suspension was centrifugated and washed with ethanol and distilled water for several times. The as-obtained powder was dried in an oven at 333 K overnight. Subsequently, the powder was calcined at 673 K for 2 hours.

Supplementary Turnover number calculations:

To investigate the TON for the 4-nitrophenol reduction over N-TiO_2@C, 10 mg catalyst was dispersed in 1.2 L 4-nitrophenol (40 ppm). Then 120 mg of $NaBH_4$ was added into the suspension. After 5 hours reaction, the 4-nitrophenol was completely converted to 4-aminophenol.

The amount of substance n_1=0.3453 mmol

For the N-TiO_2@C composite:

The nitrogen dopants are determined to be the active sites for 4-NP reduction, which has been discussed in the “origin of unexpected catalytic activity” in the manuscript.

The nitrogen dopants in TiO_2 are determined to be 4.30 at%, according to the XPS analysis.

The amount of substance TiO_2: n_2=10 mg×0.7265/(80 g/mol)=0.0908 mmol

The amount of nitrogen dopants in TiO_2 are determined to be n_3=0.0908 mmol×4.30 at%=0.0039 mmol

The nitrogen dopants in carbon are determined to be 4.64 at%, according to the XPS analysis.

The amount of substance carbon: n_4= 10 mg×0.2476/(12 g/mol)=0.2063 mmol

The amount of nitrogen dopants in carbon are determined to be n_5=0.2063 mmol× 4.64 at%=0.0096 mmol

For nitrogen doped TiO_2, the turnover number: **n** = 0.3453 / 0.0039= 88.5384

For nitrogen doped carbon, the turnover number: **n** =0.3453 / 0.0096= 35.9688

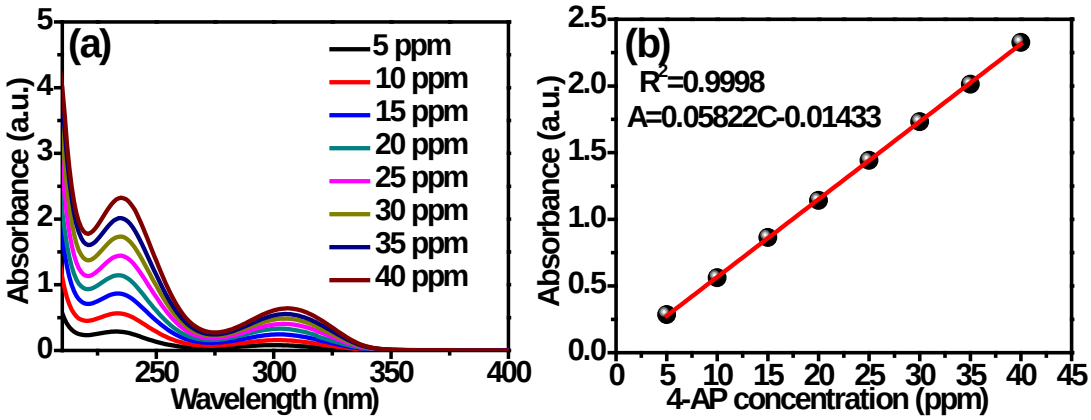

Figure S16. Absorbance and concentration of 4-aminophenol. (a) UV-visible spectra of different concentration of 4-aminophenol; (b) the relationship between the absorbance (A) and concentration (C) of 4-aminophenol (4-AP) determined by montoring changes of the featured absorption peak at ~232 nm.

Note: The absorbance of 4-AP at 232 nm in the UV-vis spectrum is 1.078 after 10 min catalytic reaction in the presence of TiO_2-C (20 ppm 4-NP). Therefore, the selectivity of 4-AP is determined to be 97% based on the linear relationship (A=0. 0.05822C-0.01433) between the absorbance (A) and the concentration (C) at 232 nm for 4-AP (**Figure S12a, b**).

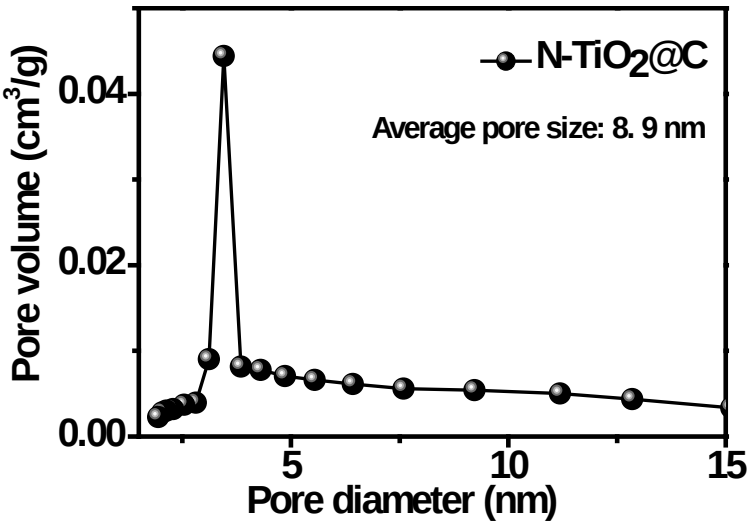

Figure S17. The pore size distribution of N-TiO_2@C.

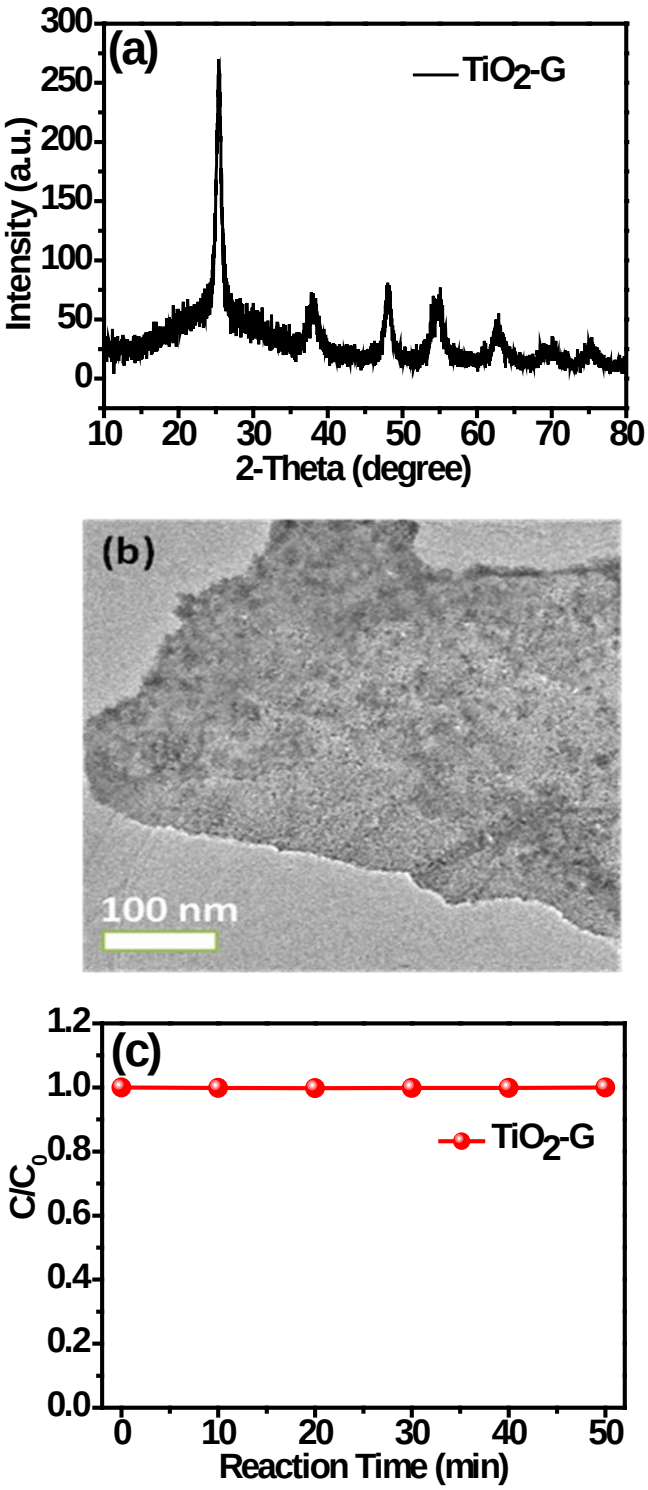

Figure S18. Characterization and catalytic activity of TiO_2-G. (a) XRD pattern. (b) TEM image. (c) Catalytic reduction of 4-nitrophenol at 298 K.

Note: TiO_2-G is prepared using the same procedure for TiO_2-NS while C_3N_4 template is replaced by graphene.

Table S2. The surface area and porosity of the TiO_2-B, TiO_2-G and N-TiO_2@C samples.

Sample	S_{BET} (m^2/g)	Average pore size (nm)	Pore volume (cm^3/g)
TiO_2-B	0.2	--	--
TiO_2-G	47	6.6	0.11
N-TiO_2@C	99	10.1	0.16

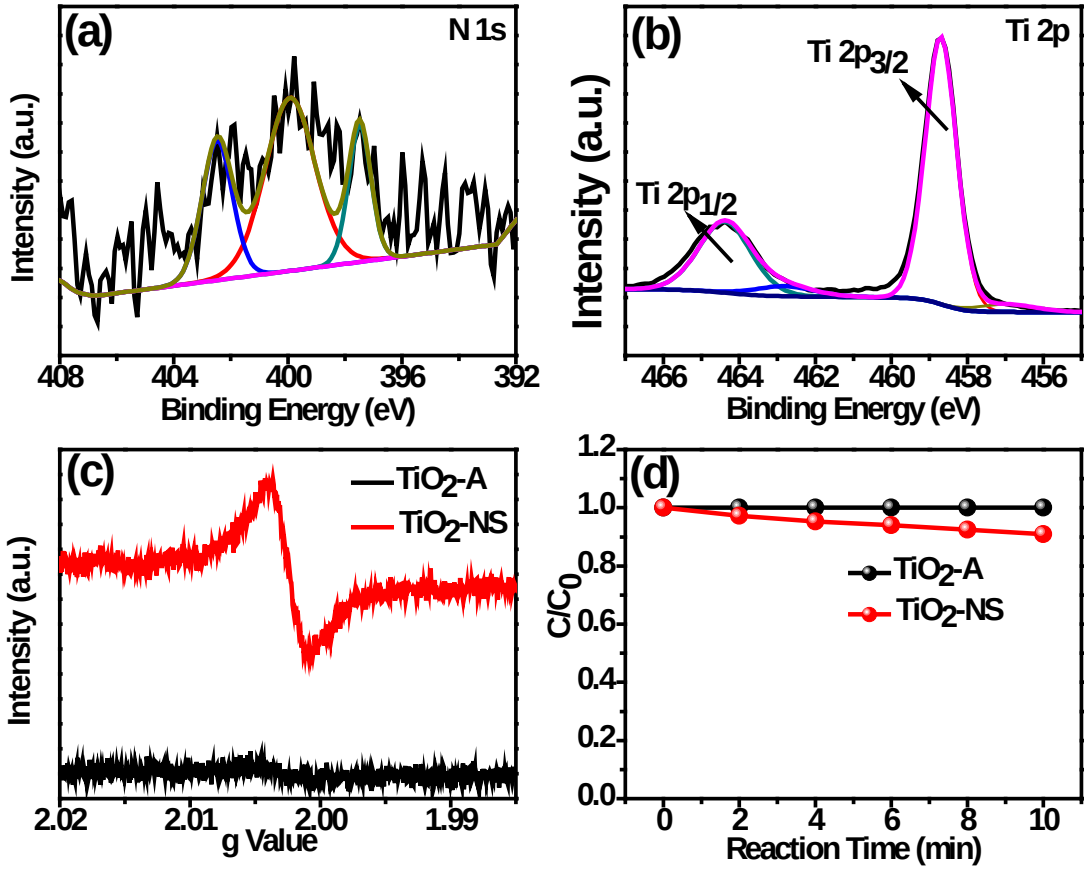

Figure S19. Characterization and catalytic activity of the TiO_2-NS and TiO_2-A. X-ray photoelectron spectra of N 1s (a) and Ti 2p (b) of the TiO_2-NS. (c) ESR spectra of the TiO_2-A and TiO_2-NS. (d) 4-nitrophenol reduction test upon TiO_2-A and TiO_2-NS at 298 K.

Note: Figure S14a shows the high-resolution XPS spectra for the N 1s region of sample TiO_2-NS. The N 1s region can be fitted into three peaks located at 397.4, 399.7 and 402.4 eV, which can be attributed to the binding energy of the N atom in the chemical bond of N-Ti-N, O-Ti-N, and Ti-N-O, respectively. The Ti $2p_{3/2}$ peak for TiO_2-NS can be decomposed into two peaks located at 458.7 and 456.9 eV, which can be assigned to Ti-O and Ti-N, respectively (**Figure S14b**).

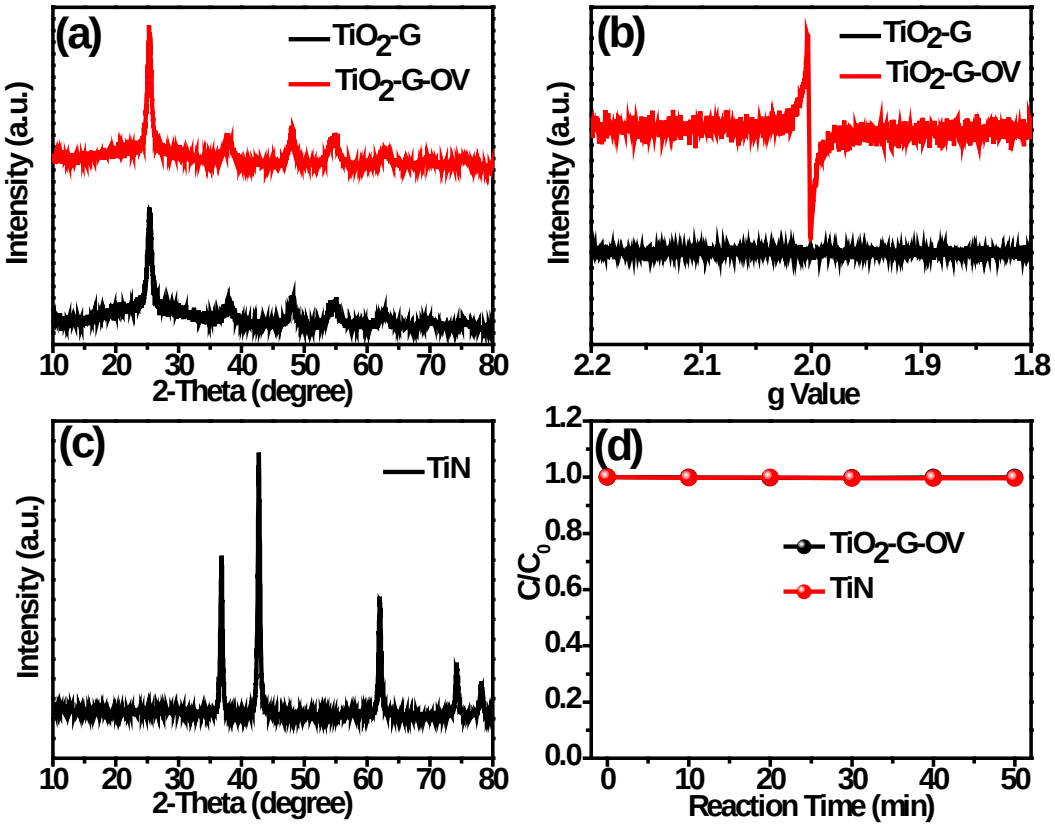

Figure S20. Characterization and catalytic activity of the samples. (a) The XRD patterns of the TiO_2 nanosheets prepared using graphene template (TiO_2-G) and TiO_2-G with oxygen vacancy (TiO_2-G-OV). (b) ESR spectra of the TiO_2-G and TiO_2-G-OV; (c) The XRD patterns of the commercial available TiN nanoparticles; (d) 4-nitrophenol reduction test upon TiO_2-G-OV and TiN at 298 K.

Note: TiO_2-G is prepared using the same procedure for TiO_2-NS while C_3N_4 template is replaced by graphene. TiO_2-G-OV is prepared according to our previous report [*Appl. Catal., A* **2013,** *459* (0), 34-40]. Briefly, 0.1 g TiO_2-G was dispersed in 10 mL benzyl alcohol solution. Then, the suspension was irradiated by a Xe lamp with a UV light band-pass filter (λ=365±15 nm) under vigorous stirring for 2 hours. Then, the suspension was centrifugated and washed with ethanol for several times. After that, the sample was dried in an oven at 333 K overnight.

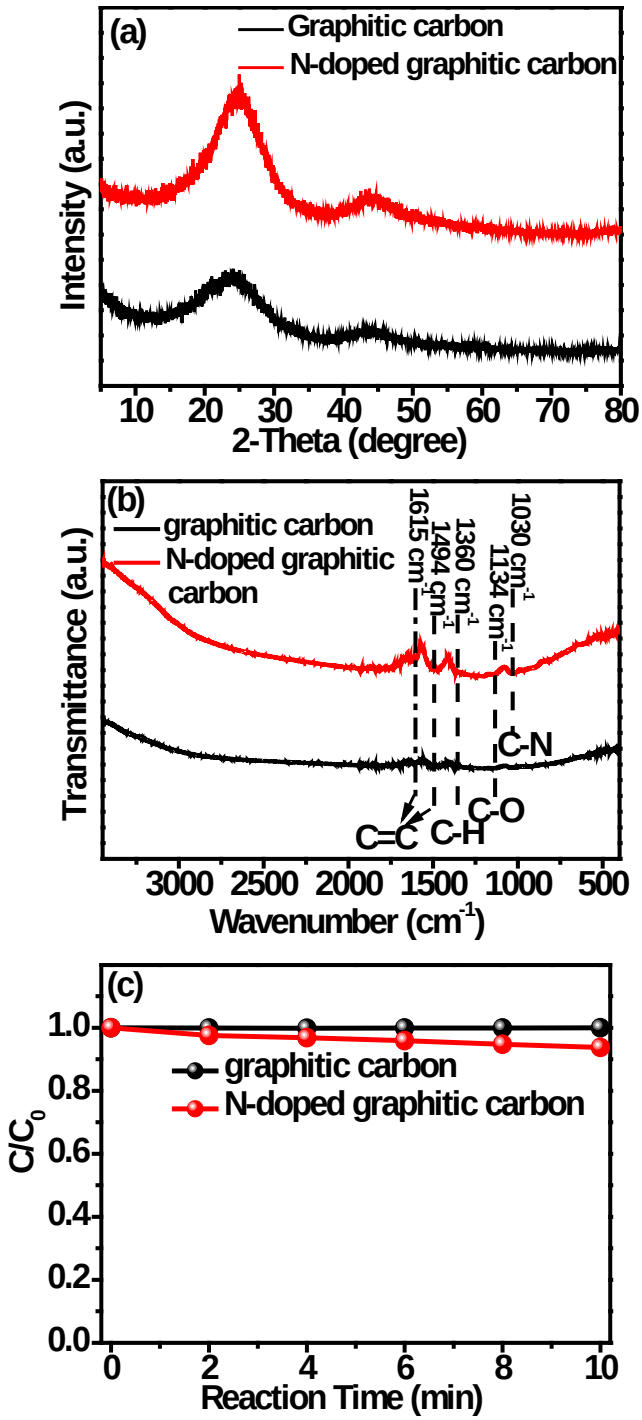

Figure S21. Characterization and catalytic activity of graphitic carbon and nitrogen doped graphitic carbon. (a) XRD patterns. (b) FTIR spectra. (c) 4-nitrophenol reduction test at 298 K.

Note: The graphitic carbon was synthesized by calcining the glucose (1.0 g) at 800 ^{o}C for 2 hours under N_2 atmosphere. The nitrogen-doped carbon was synthesized by

calcining the glucose (1.0 g) and melamine (0.1 g) at 800 ^{o}C for 2 hours under N_2 atmosphere.

Scheme S1. Proposed reduction processes of nitroaromatics over N-TiO_2@C in the presence of $NaBH_4$.

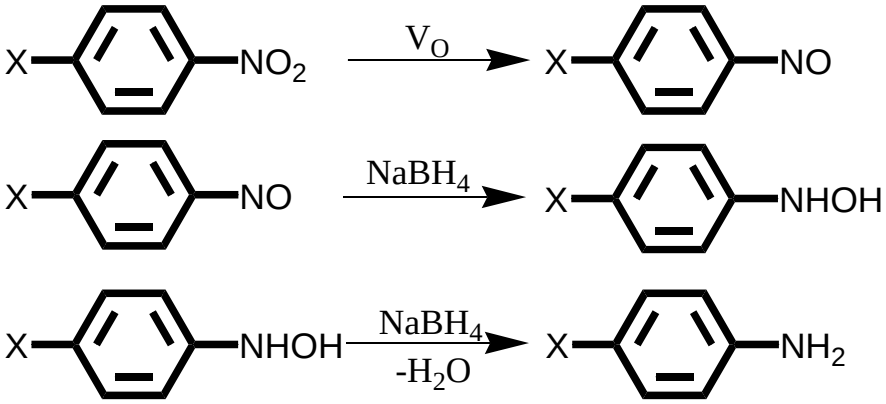

Here, V_O represents the oxygen vacancy on TiO_2.